Geophysical Journal International

Geophys. J. Int. (2024) **239,** 821–840
Advance Access publication 2024 August 20
GJI Seismology

https://doi.org/10.1093/gji/ggae289

Automatic relocation of intermediate-depth earthquakes using adaptive teleseismic arrays

Alice Blackwell [1], Timothy Craig [2] and Sebastian Rost [1]

[1] *Institute for Geophysics and Tectonics, School of Earth and Environment, University of Leeds, Leeds, UK. E-mail: ee18ab@leeds.ac.uk*
[2] *COMET, Institute for Geophysics and Tectonics, School of Earth and Environment, University of Leeds, Leeds, UK*

Accepted 2024 August 16. Received 2024 July 18; in original form 2024 January 9

SUMMARY

Intermediate-depth earthquakes, accommodating intraslab deformation, typically occur within subduction zone settings at depths between 60–300 km. These events are in a unique position to inform us about the geodynamics of the subducting slab, specifically the geometry of the slab and the stress state of the host material. Improvements in the density and quality of recorded seismic data enhance our ability to determine precise locations of intermediate-depth earthquakes, in order to establish connections between event nucleation and the tectonic setting. Depth phases (near-source surface reflections, e.g. *pP* and *sP*) are crucial for the accurate determination of earthquake source depth using global seismic data. However, they suffer from poor signal-to-noise ratios in the *P* wave coda. This reduces the ability to systematically measure differential traveltimes to the direct *P* arrival, particularly for the frequent lower magnitude seismicity which highlights considerable seismogenic regions of the subducted slabs. To address this limitation, we have developed an automated approach to group globally distributed stations at teleseismic distances into *ad-hoc* arrays with apertures of 2.5°, before optimizing and applying phase-weighted beamforming techniques to each array. Resultant vespagrams allow automated picking algorithms to determine differential arrival times between the depth phases and their corresponding direct *P* arrival. Using these differential times we can then determine the depths of earthquakes, which in turn can be used to create a catalogue of relocated events. This will allow new comparisons and insights into the governing controls on the distribution of earthquakes in subducted slabs. We demonstrate this method by relocating intermediate-depth events associated with northern Chile and the Peruvian flat slab regions of the subducting Nazca plate. The relocated Chilean catalogue contains comparable event depths to an established catalogue, calculated using a semi-automated global methodology, which serves to validate our fully automatic methodology. The new Peruvian catalogue we generate indicates three broad zones of seismicity approximately between latitudes 1–7°S, 7–13°S and 13–19°S. These align with flat to steep slab dip transitions and the previously identified Pucallpa Nest. We also find a regionally deeper slab top than indicated by recent slab models, with intraslab events concentrated at points where the slab bends, suggesting a link between slab flexure and intermediate-depth earthquake nucleation.

Key words: South America; Time-series analysis; Seismicity and tectonics; Subduction zone processes.

1 INTRODUCTION

Intermediate-depth earthquakes – those with hypocentral depths between 60–300 km – occur in all actively subducting slabs (e.g. Frohlich 2006) and, although they comprise only a small proportion of the total seismic moment release associated with subduction zones, they can present a significant seismic hazard of the overlying population centres (Abe 1972; Beck *et al.* 1998). Despite this, they remain one of the least-well understood types of earthquake, with open questions as to what controls their occurrence, distribution and nucleation (Hacker *et al.* 2003; Frohlich 2006; Ferrand *et al.* 2017; Hosseinzadehsabeti *et al.* 2021). One of the principal issues limiting our understanding of such earthquakes is the difficulty in accurately locating these earthquakes, and their relationship to the rheology, geometry and structure of the host slab. Determining accurate locations for such earthquakes, particularly in regions with

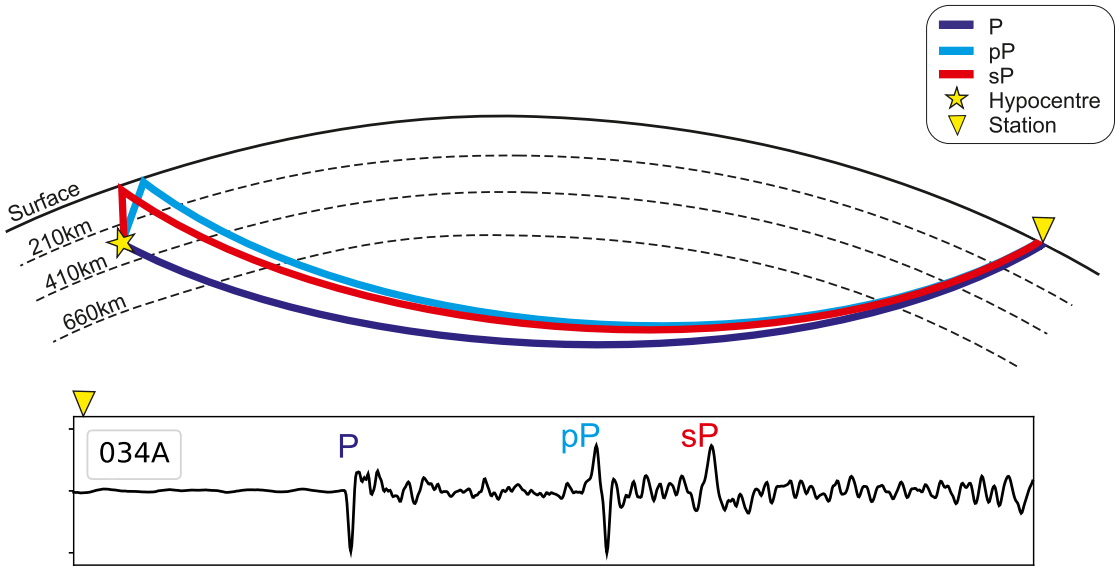

Figure 1. 2-D schematic of the *P*, *pP* and *sP* ray paths from an earthquake hypocentre (star) to a teleseismic receiver (triangle), and an example vertical component, velocity waveform from station 034A of the TA network. The waveform is taken from the 2010 May 23, m_b 6.2 event located at (−13.98, −74.37).

little near-field seismic instrumentation can be difficult, and subject to significant uncertainty. Earthquake depth, in particular, is of great importance, as both rheological properties and intraslab stress change fastest in the vertical direction, with the greatest complexity in seismogenic structure.

For global earthquake location, a vital observation offering both a direct and an independent constraint on the depth of an earthquake is the relative delay time of teleseismic depth phases (Fig. 1) – near-source surface reflections (*pP* and *sP*), which otherwise follow a similar ray path to the associated direct phase (*P*). The relative delay time of these depth phases is dependent on depth of the earthquake below the overlying surface and the near source velocity structure. Hence, in cases where the velocity structure is reasonably well known, the delay time offers a precise constraint on earthquake hypocentral depth, which is independent of the absolute traveltime of any of the various phases. Therefore, depth determination using the relative arrival times is unaffected by any velocity structure variations outside of the near-source region, and additionally independent of the lateral location.

However, for smaller earthquakes ($M_w < 6$), depth phases are often difficult to identify – depth phase detection is hindered by their relatively low amplitude, and by the increased background 'noise' levels present in the direct phase coda, particularly for earthquakes in areas with complex near-source velocity structures. The recorded amplitude of the arrivals depends upon factors such as the moment magnitude, radiation pattern and the attenuation during transmission from source to receiver. Additionally, higher magnitude events at shallower depths are likely to have longer source durations and shorter relative delay times between the phases, which can result in the depth phases and the direct arrival overlapping and interfering with each other, further hindering identification.

One approach has been to enhance the detectability of depth phases by stacking waveform data where depth phases are coherent – an approach commonly employed using data from the limited number of small aperture arrays (typically $< 0.4^\circ$ or 50 km) around the world (e.g. Heyburn & Bowers 2008; Craig & Heyburn 2015) via beamforming. Other approaches have tried to apply either time-compression or distance-dependent windowing of the waveform to allow the stacking of data from wide aperture (typically these can be $> 9^\circ$ or 1000 km) or global arrays (Woodgold 1999; Murphy & Barker 2006; Tibuleac 2014; Craig 2019; Fang & Van Der Hilst 2019). However, with the increasing station density of long-term seismic networks, more recent approaches have been developed which construct 'medium' aperture (typically $< 5^\circ$ or 556 km; Florez & Prieto 2017) seismic arrays, which suffer from neither the geographic sparsity of small-aperture arrays, nor the coherence limits of wide-aperture arrays. With the rapid increase in station density across many continental regions, the construction of large numbers of medium-aperture arrays is now possible for many, if not all, contemporary earthquakes, and offers a vital avenue to greatly increase the number of depths phases observed in global seismic catalogues, and to greatly improve the location of intermediate depth earthquakes, in particular.

Approaches to the accurate determination of earthquake depths tend to divide into two groups: those using the pre-identified arrival times of specific seismic phases (including depth phases; e.g. Engdahl *et al.* 1998; Bondár & Storchak 2011; Münchmeyer *et al.* 2023), and those determining location parameters through the inversion of waveform data (over a window encompassing the depth phases; e.g. Craig *et al.* 2011; Devlin *et al.* 2012; Craig & Hull 2024). In general, the latter has required significant computational and analytical resources, and has largely been restricted to studies of specific events, seismic sequences, or carefully defined regions, whilst the former forms the basis for most global earthquake catalogues. Here, we instead aim to automate an innovative hybrid approach to waveform processing to greatly increase the number of depth phases for which relative traveltimes can be determined.

In this paper, we demonstrate a dynamic and fully automated approach to relocate the hypocentres of intermediate-depth earthquakes in depth using the relative delay times between the *P* wave and its associated depth phases (*pP* and *sP*). The approach leverages the increasing abundance of teleseismic data to allow the construction of adaptive teleseismic seismic arrays, which aim to image and detect clear depth phases for smaller magnitude events. We start by illustrating our processing workflow (see Section 2) using an

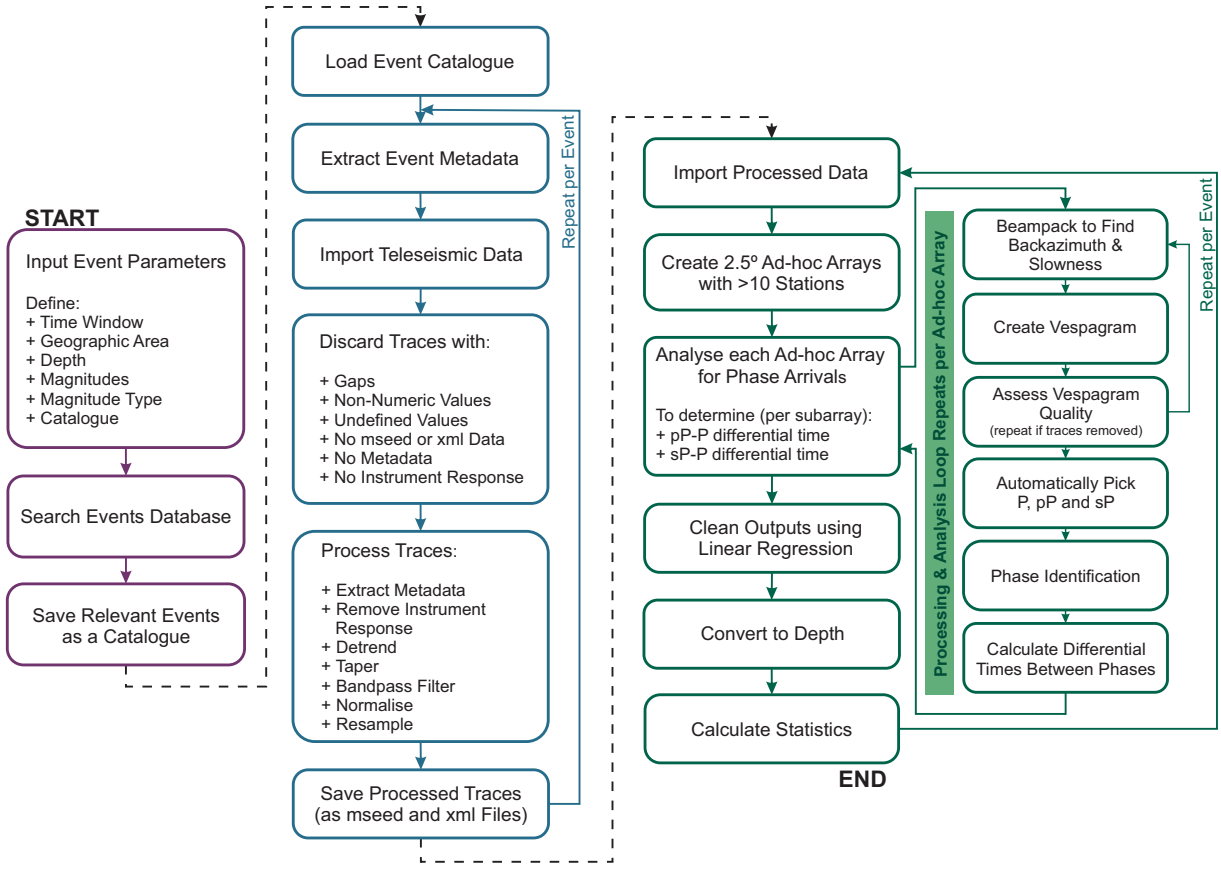

Figure 2. Workflow summarizing the key steps of the method. Purple outlined boxes (left column) indicate processes related to assembling the event catalogue, blue outlined boxes (middle left column) indicate processes related to teleseismic data loading and pre-processing, and green outlined boxes (middle right and right columns) indicate processes related to depth determination.

example earthquake from Peru, then presenting comparisons with previous depth-phase derived catalogues from northern Chile (see Section 3), before showing a regional case study based on the Peruvian subduction zone (see Section 4).

2 RELOCATION ALGORITHM

To relocate intermediate-depth earthquakes automatically, we create dynamic medium-aperture *ad-hoc* arrays, independently generated to optimize usage of the available teleseismic data for each earthquake (see Section 2.3), detect and automatically pick the *P*, *pP* and *sP* phases from signal-to-noise enhanced vespagrams (see Section 2.4) and convert the *pP–P* and *sP–P* relative times to depth (see Section 2.5). This builds upon the methodology outlined in Florez & Prieto (2017).

The approach presented here can be used to create a high-resolution, regional intermediate-depth earthquake catalogue using depth phases. The primary aim is the determination of event catalogues for intermediate-depth earthquakes in subduction zones, but our approach maintains the scope to handle deeper earthquakes in the continental crust, provided a clear separation between the direct arrival and depth phases is present (Wimpenny *et al.* 2023). Globally, there are many regions which do not possess dense, local seismic networks and therefore lack near-field data for the constraint of earthquake location – a problem particularly prevalent in remote or oceanic subduction settings – and it is in these settings that we anticipate the method presented here will be particularly impactful. Fig. 2 shows the workflow of our approach, which we will discuss in the upcoming sections.

2.1 Selecting events

To select candidate earthquakes for relocation, we start from a preliminary earthquake catalogue containing event locations, times and magnitudes. For the examples in this section, we use the International Seismological Centre (ISC) catalogue post-1995, with a search box over Peru, a depth range of 40–350 km and a magnitude range of m_b 3.0–6.5. We begin with a catalogue which extends into magnitudes well below where we would typically expect to detect depth phases and with a larger depth range, in order to determine a lower magnitude limit for our approach (see Section 4.1), and test the ability of our approach to handle shallower and deeper depth data. For the upper magnitude limit, we choose a m_b 6.5 cut-off because we feel that more impact will be achieved by focusing on relocating smaller, less well constrained events – for earthquakes larger than this, depth phases are typically detectable in single-station data. Restricting the relocation of upper magnitude events also limits the application of a point source assumption, as larger earthquakes are more likely to consist of complex fault plane mechanics and multiple areas of slip.

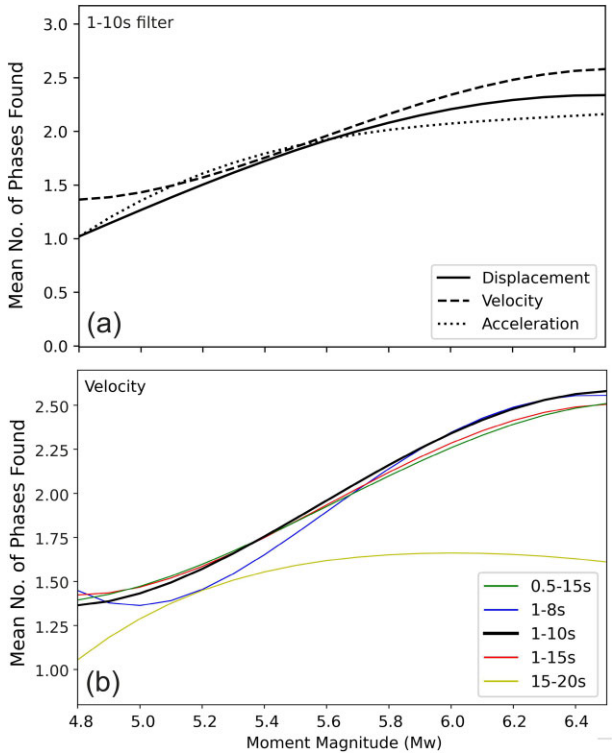

Figure 3. Mean number of phases (*P*, *pP* or *sP*) found per moment magnitude, provided by the Global Centroid Moment Tensor Project (GCMT) catalogue (Dziewonski *et al.* 1981; Ekström *et al.* 2012), whilst (a) applying a 1–10 s bandpass filter for three seismic data types — displacement, velocity and acceleration, and (b) applying five bandpass filters to velocity data.

2.2 Data and data processing

For a given earthquake from the event catalogue (Section 2.1) we take all available vertical component station data recorded on channels BH and HH at teleseismic distances (30–90° epicentral angle) from the initial location, from all of the open access FDSN (International Federation of Digital Seismograph Networks) data centres (see Data Availability section). We limit our station selection to those existing at teleseismic distances to allow sufficient time for the depth phase arrivals from intermediate-depth earthquakes to separate, whilst limiting the interference of upper mantle reflections and triplications.

Individual waveforms are limited to 200 s before the event origin time to 1500 s after, and subsequently checked and discarded automatically if there are incomplete traces, missing metadata or instrument responses. All remaining waveforms have their instrument response deconvolved, leaving the data recorded in units of velocity, are linearly detrended, tapered at 5 per cent of the trace length, bandpass filtered between 1–10 s using a three-corner Butterworth filter, resampled to 10 Hz and normalized to their peak amplitude (see Fig. 2). The final quality checked data will be dynamically grouped into medium-aperture *ad-hoc* arrays (see Section 2.3).

2.2.1 Determination of optimal filter parameters

We determine an optimum combination of bandpass filter (1–10 s) and seismic data (velocity) by testing five filter ranges on all three types of data (displacement, velocity or acceleration) for approximately 470 Peruvian intermediate-depth earthquakes and assessing the performance of our automatic phase picking routine (see Sections 2.4.4 and 2.4.5). The five test bandpass filter ranges were 0.5–15, 1–8, 1–10, 1–15 and 15–20 s, and were initially selected based upon the source-time function wavelengths with respect to magnitude included in the SCARDEC (Seismic source ChAracteristics Retrieved from DEConvolvolving teleseismic body waves) database (Vallée & Douet 2016). We ran the relocation algorithm from data processing (see Section 2.2) to phase identification (see Section 2.4.5) for each earthquake using all combinations of the test conditions, and recorded the number of phases identified per *ad-hoc* array (with a maximum of 3 for detecting *P*, *pP* and *sP*).

The results indicate that the automated phase picking routine is affected by the seismic data type, demonstrating a significantly better performance using velocity data (Fig. 3a), particularly towards the lower and upper bounds of the tested earthquake magnitudes. However the detection of depth phases for a given magnitude has a low sensitivity to the tested bandpass ranges, except the 15–20 s filter which is used to appraise sensitivity of the results when given an unlikely filter (Fig. 3b). It is apparent that the addition of waveforms with 10–15 s periods provides a marginal advantage for picking at magnitudes less than 5.4, and a marginal disadvantage at magnitudes greater than 5.4. Whilst filtering out waveforms in the range of 8–10 s reduces the mean number of phases picked between magnitudes 4.9 and 5.7. The 1–10 s filter provides a more consistent result over the entire range of magnitudes, and is therefore used for processing data for our relocation methodology. An adaptive filter dependent upon magnitude has been tested, but offers little improvement over the best-fitting filter for the range of magnitudes we are considering. More results from testing for the optimal filter parameters are included in Supporting Information, see Figs S1 and S2.

2.3 *Ad-hoc* arrays

Our approach, comparably to others (Tibuleac 2014; Florez & Prieto 2017; Craig 2019; Fang & Van Der Hilst 2019), relies on the application of array processing techniques to groups of teleseismic stations, to boost the signal-to-noise ratio of the depth phases, and increase the likelihood of detection. Craig (2019) stacks global teleseismic data using a kurtosis detected *P* wave arrival, whilst Fang & Van Der Hilst (2019) autocorrelate and beamform their global teleseismic traces using a simple moveout correction to a reference epicentral distance. Although both of these methods use a global distribution of data, there is limited scope to account for local to receiver path variations due to 3-D velocity structure. Florez & Prieto (2017) and Tibuleac (2014) both beamform for a small number of fixed medium-aperture subarrays/wide-aperture superarrays of teleseismic stations constructed for western USA, Florez & Prieto (2017) also construct arrays for western Japan. The use of defined arrays provides an opportunity to individualize beamforming to the local 3-D velocity structure, by allowing data-driven determination of the local to array slowness and backazimuth parameters, resulting in an improved beam – see Section 2.4.1. However, the distribution of stations reporting at teleseismic distances for any given earthquake varies due to temporary deployments and the steady increase in stations over time. Hence, instead of defining a small number of fixed arrays, we incorporate an algorithm for the dynamic creation of an optimum suite of medium-aperture *ad-hoc* arrays from the

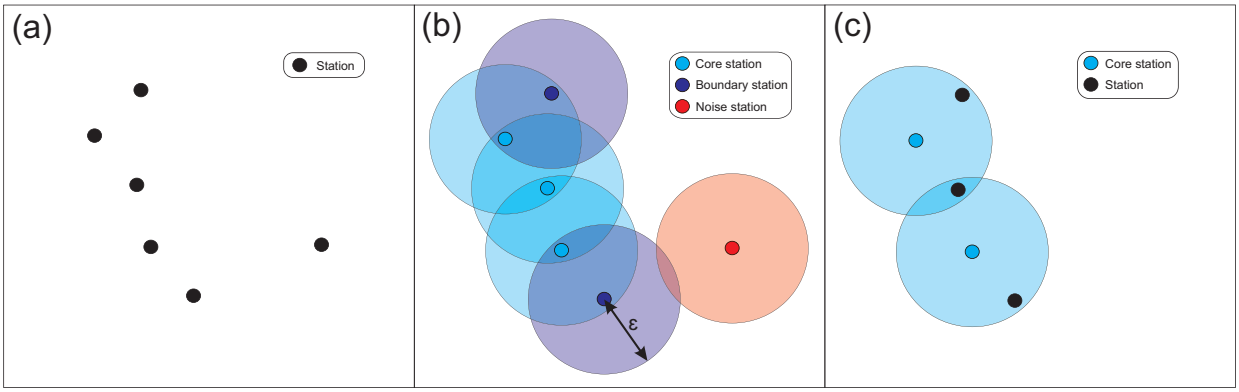

Figure 4. Cartoon illustrating how we dynamically create *ad-hoc* arrays from a population of stations. (a) Initial set of stations to divide into *ad-hoc* arrays. (b) How the DBSCAN clustering routine assigns core, boundary and noise labels to the stations, assuming that the minimum number of points required in the neighbourhood within a search radius ε of a core point is 3. (c) Shows how the 'noise' stations have been removed from the data set, and only the mutually exclusive core stations are retained to create well-spaced and well-populated *ad-hoc* arrays using the Ball-Tree routine.

initial teleseismic population of stations unique to each earthquake. We also determine the optimum beamforming parameters and automated picking threshold per *ad-hoc* array (see Sections 2.4.1 and 2.4.4).

We group stations with waveform data which has successfully passed our data quality control and pre-processing (see Section 2.2) into medium aperture *ad-hoc* arrays (see Fig. 2) using a combination of two unsupervised machine learning algorithms – DBSCAN (Density-Based Spatial Clustering of Applications with Noise) and Ball-Tree nearest neighbour functions (Pedregosa *et al.*, 2011) — in a process proposed by Ward *et al.* (2023).

DBSCAN clustering (Ester *et al.* 1996) categorizes data points into either clusters or noise depending upon whether the point is part of a neighbourhood based on a set minimum density of points. The minimum density is defined using a given radius (ε) and a given minimum number of points, to remove stations which are not densely clustered enough to be considered for a medium aperture *ad-hoc* array (noise). The stations which are retained as part of a cluster are additionally categorized into core or boundary points (Fig. 4). Core points possess the specified minimum number of points within the given radius of itself (i.e. core stations in Fig. 4 have three stations within their radius), whilst boundary points do not. The stations which are core or boundary points are retained for the Ball-Tree algorithm to divide into *ad-hoc* arrays.

We then use the Ball-Tree nearest neighbour algorithm (Omohundro 1989) to identify the stations (core or boundary) located within the given radius from each core station, each core station and its associated stations then become an *ad-hoc* array. The use of the Ball-Tree algorithm in this way results in overlapping *ad-hoc* arrays, where the core station of one *ad-hoc* array is contained within the radius of other core station's array clusters. A further process weeds out the excess *ad-hoc* array cores and associated stations, thus leading to a series of *ad-hoc* arrays where core stations are mutually exclusive and non-core stations can be shared (Fig. 5). The data are then re-organized to reflect the newly found *ad-hoc* array groupings. We have tested this routine on regional and global distributions of seismic stations, with success on both counts.

We test the *ad-hoc* array creation process for a range of apertures (array diameter) from 167 to 2222 km. Given a 1–10 s bandpass filter, 167 km is approximately the smallest *ad-hoc* array aperture we can consider for our target frequency, since the array aperture should be larger than the longest wavelength of interest in order to form a meaningful beam. If the wavelength is larger than the array aperture, the array has a limited wavenumber (or slowness) resolution and the array, essentially, acts as a single station (Schweitzer *et al.* 2012). This significantly limits array processing benefits such as an improvement in signal-to-noise ratio. Conversely using a wider array aperture increases the risk of larger velocity structure variations within the array, which increases the probability that higher frequency, shorter wavelength arrivals will stack incoherently. We observe that whilst the traces in the *ad-hoc* arrays coherently stack well between apertures of 167 km and approximately 1333 km, there is a trade-off between the number of *ad-hoc* arrays created, the proportion of stations used, and the *ad-hoc* array aperture considered.

We find that *ad-hoc* arrays with a 278 km (2.5°) aperture strike the best balance between maintaining a plane wave assumption across the included stations (see Fig. S3 in Supporting Information), and maximizing the number of *ad-hoc* arrays that can be created from the station distribution available. Requiring at least 10 stations per array ensures the wavefield is sampled sufficiently and that there are enough traces in the array to enable acceptable signal-to-noise improvement. Note that the assigned array diameter represents a maximum aperture, the *ad-hoc* arrays created likely contain stations within a smaller area. For the remainder of the approach, we use 278 km as the maximum aperture for our arrays, expect at least 10 stations in each array and set the geometric centre of each *ad-hoc* array as the 'reference station'.

2.4 Array processing

Once our station population has been divided into *ad-hoc* arrays (see Section 2.3), each *ad-hoc* array is then passed through an array processing and analysis loop, aiming to boost signal-to-noise ratio sufficiently enough for the depth phases to be automatically picked, identified and their differential arrival times to be calculated (see Fig. 2). The differential times found per *ad-hoc* array are collected together to determine a final hypocentral depth (see Section 2.5).

2.4.1 Determining optimum beamforming parameters

Beamforming involves the alignment, stacking and normalization of an array of seismic traces to enhance the amplitude of smaller amplitude arrivals, such as depth phases. In this section, we adopt *P*

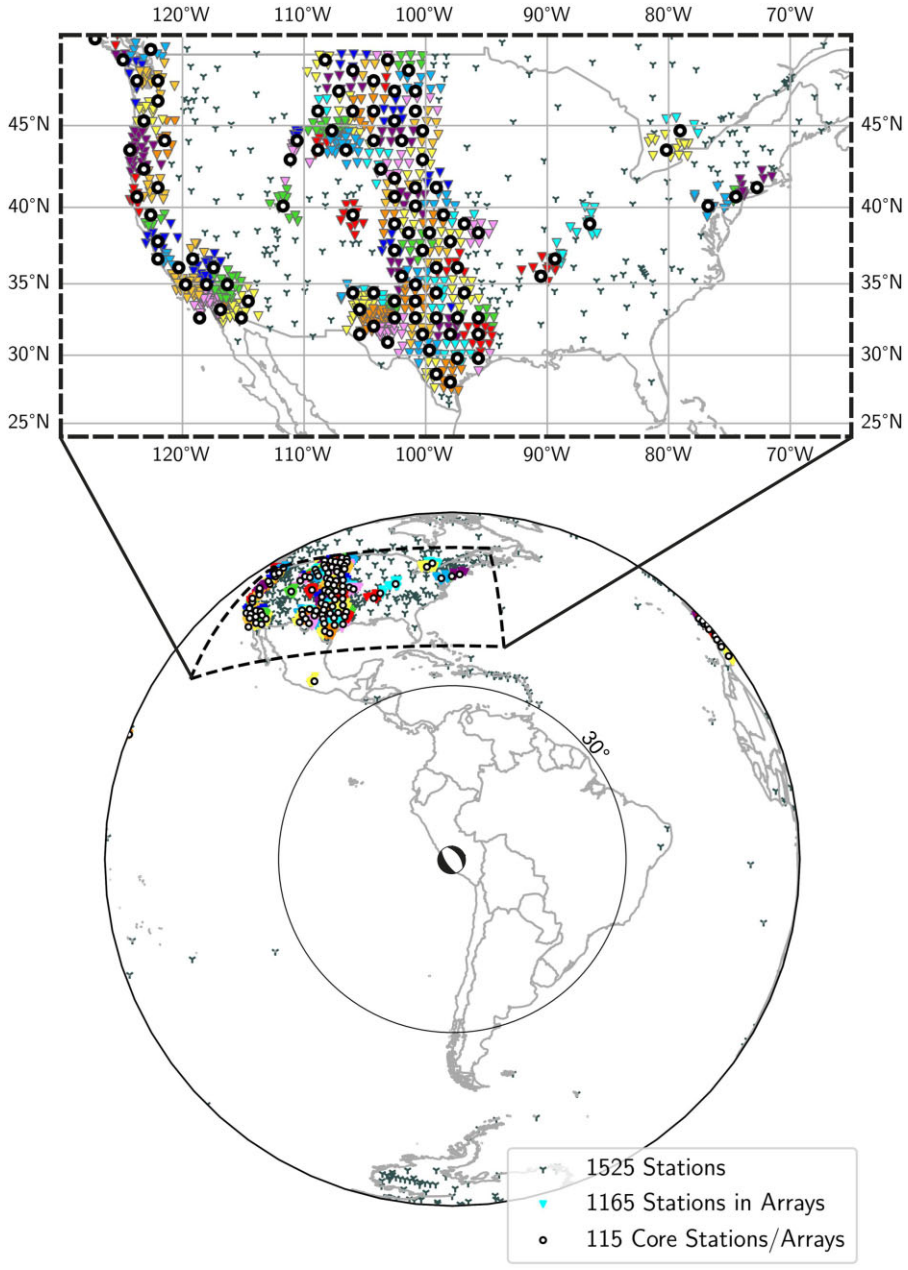

Figure 5. Example of the *ad-hoc* array creation process for a m_b 6.2 event from 2010 May 23 located in the Peruvian flat slab portion of the Nazca plate, showing a global distribution of teleseismic stations and the subsequent *ad-hoc* arrays on the bottom, and a zoom in of the *ad-hoc* arrays created in the USA on the top. The core stations are shown as thick black circles and the associated *ad-hoc* array stations as coloured triangles. The unused stations (grey Ys) are those removed via the DBSCAN routine, prior to the Ball-Tree process. The earthquake focal mechanism is taken from the GCMT catalogue (Dziewonski *et al.* 1981; Ekström *et al.* 2012).

wave beamforming to determine the optimum backazimuth and slowness parameters directly from the *ad-hoc* array trace data, to be used when beamforming the depth phases later in Section 2.4.2. This process, as we show, is particularly important for the dynamic medium-aperture *ad-hoc* arrays we construct, as it compensates for the locally-variable velocity structure below each array.

The beamforming process can be applied to an array of waveforms using:

$$b(t) = \frac{1}{M}\sum_{i}^{M} x_i(t - \mathbf{r}\cdot\mathbf{u}), \tag{1}$$

where M is the number of stations, x_i is the recorded trace at station i, $\mathbf{r}$ is a two-component vector describing the location of station i relative to the reference station and $\mathbf{u}$ is a two-component horizontal slowness vector. The dot product of $\mathbf{r}$ and $\mathbf{u}$ represents the timeshift a trace needs to undergo in order to align its expected phase arrivals with those from the reference location, to stack coherently.

The beam is formed for a specific horizontal slowness and backazimuth, assuming the propagation of a plane wavefront across the array – this is a good approximation for the chosen array size. Theoretical values for the slowness and backazimuth can be calculated using the relative location of the earthquake source to the

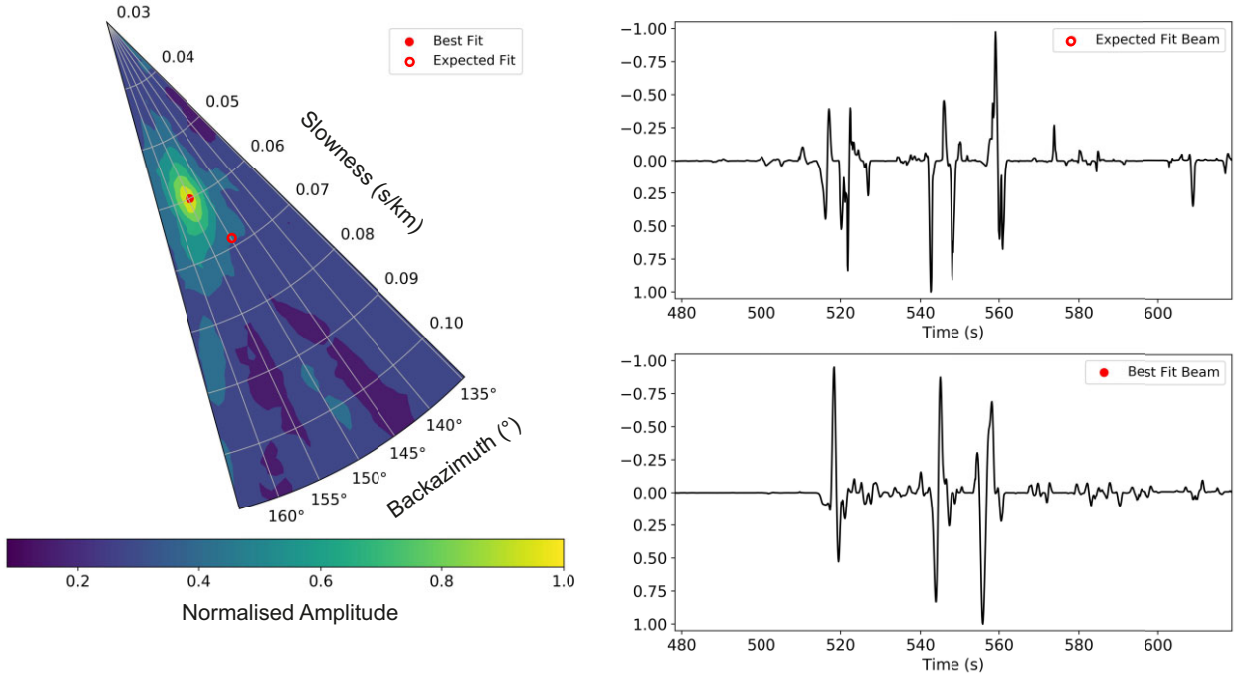

Figure 6. *P* wave amplitude during beamforming in polar coordinates (backazimuth and slowness) to determine the best-fitting backazimuth and slowness parameters directly from the *ad-hoc* array traces. The open red circle shows the theoretical slowness and backazimuth found through calculation and the corresponding phase-weighted beam to the top right. The filled red circle shows the beampack derived values and the resultant phase-weighted beam to the bottom right, showing the importance of measured backazimuth and slowness values. Example from m_b 6.2 event on 2010 May 23, *ad-hoc* array at 49.2° epicentral distance.

reference location, and assuming propagation along a great circle path, combined with ray tracing through an assumed 1-D velocity structure. Alternatively, a process such as F-K (frequency-wavenumber) analysis or beampacking can be used to determine optimal, locally-calibrated values for arrivals from a given earthquake (Rost & Thomas 2002; Florez & Prieto 2017). Beampacking is the time domain equivalent to F-K analysis and searches over a grid of slowness and backazimuths for beamforming, to determine the values which produce the beam with maximum amplitude within a selected time window (typically centred on a specific phase arrival).

To directly extract the optimal slowness and backazimuth values from each *ad-hoc* array, we perform beampacking on a narrow time window centred on the predicted direct *P* wave arrival. The traces are trimmed to 17 s time windows around the predicted *P* arrival time calculated using the ak135 1-D Earth model (Kennett *et al.* 1995), and beamformed relative to the reference station of the *ad-hoc* array according to eq. (1). The length of the time window has been found by trial and error, it aims to preserve the *P* arrival and exclude minimally separated depth phases from shallower events, whilst allowing a margin of error in the modelled *P* arrival time due to 3-D velocity structure. We test a 30×30 grid of backazimuth and slowness values during our beampacking routine, the ranges of which are centred upon the theoretical backazimuth and slowness values. For backazimuth, the tested values range from the geodetic backazimuth value $\pm$ 15° in 1° intervals, whilst slowness is tested from the modelled slowness value $\pm$ 0.015 s/km in intervals of 0.001 s/km.

The maximum amplitude of each beam (assumed to be the *P* arrival) is extracted and mapped onto a polar grid, with slowness displayed along the radius and backazimuth given by the bearing (Fig. 6). The beam providing the largest amplitude indicates the best fitting, optimal slowness and backazimuth for the event *P* arrival for the *ad-hoc* array, both values can be read directly from the plot.

We find that beams created using the data-derived, observationally constrained backazimuth and slowness values account for near-receiver velocity structure variations and the resultant 3-D ray path propagation effects, which significantly reduces impact from incoherent noise, compared to the beams constructed with theoretically derived parameters. The improvement between a beam constructed using parameters calibrated to produce maximum amplitude for the direct arrival, and one using the theoretical values can be seen in Fig. 6 (an alternative display can also be seen in Fig. S4 located in Supporting Information). The optimal backazimuth and slowness parameters found through beampacking are used for beamforming *ad-hoc* array traces in Section 2.4.2, to increase the likelihood of automatically detecting and picking depth phases.

2.4.2 *Vespagrams*

We use vespagrams to assess the quality of the *ad-hoc* array data for the automated picking routine (see Section 2.4.4, and Fig. 2). Vespagrams are an array process which display a series of beams for a range of slownesses or backazimuths (Rost & Thomas 2002).

Our vespagrams highlight the time and slowness using a fixed backazimuth where phase arrivals are most coherent, by beamforming the *ad-hoc* array per slowness using eq. (1). They are constructed using the same reference stations, test slowness range and best-fitting backazimuth found during beampacking (see Section 2.4.1). The resulting traces are stacked using phase weighting (Schimmel & Paulssen 1997) with a power of 4 to amplify the signal relative to the noise, before being asssembled into a vespagram (Fig. 7).

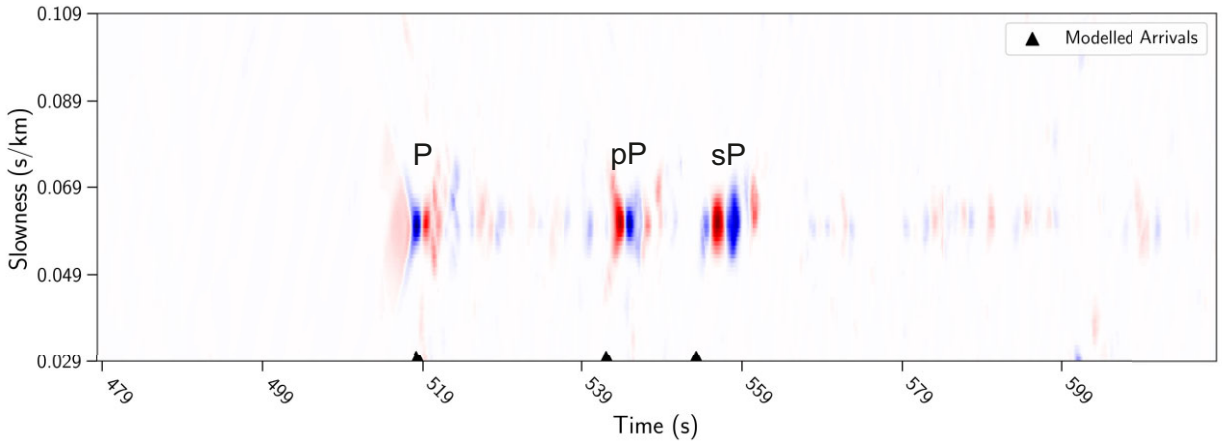

Figure 7. Normalized vespagram from an *ad-hoc* array located at an epicentral distance of 49.2°, for the m_b 6.2 event on 2010 May 23. Phase arrivals are labelled.

The resulting plot allows for the identification of the most coherent beamform, which also illustrates the time of each phase arrival, assuming that the noise is diminished enough to allow the stacked phase arrival amplitudes to display significantly. Vespagrams for each *ad-hoc* array are subject to quality control based on the clarity of signals along the expected slowness range and the overall noise content, with low-quality vespagrams being removed from the relocation process (See Section 2.4.3). Remaining vespagrams, and their *ad-hoc* arrays, are parsed to the automated picking routine (see Section 2.4.5).

2.4.3 Assessing vespagram quality

To limit the progression of poor quality *ad-hoc* arrays in order to assist the subsequent automatic picking routine (see Section 2.4.4), we apply two quality assessments to each *ad-hoc* array. The first assessment uses cross-correlation to consider the individual traces of the *ad-hoc* array relative to the beam formed using the optimal backazimuth and slowness parameters found in Section 2.4.1. The second check assesses the signal-to-noise ratio of the entire vespagram by considering the highest amplitude phases and their slowness distribution.

In order to assemble a clean *ad-hoc* array beam, traces significantly different from the beam are identified using a cross-correlation approach, and removed (see Fig. S5, Supporting Information). Each time-shifted trace is trimmed around the expected *P* wave arrival and compared to the *ad-hoc* array *P* wave arrival of the beam. A cross-correlation coefficient of greater than 0.3 is required alongside a maximum time-shift of 0.5 s for the trace to be deemed constructive to the *ad-hoc* array beam. Traces which fail to meet these criteria are discarded. Once a set of final traces is determined, the processing of the *ad-hoc* array is restarted (e.g. the beampacking derived slowness and backazimuth are re-determined). The cross-correlation check will not be repeated. The algorithm will pass over the check and continue to the construction of vespagrams for further data quality assessment. If fewer than eight traces remain in the *ad-hoc* array after the cross correlation check, the *ad-hoc* array will be removed from analysis.

For the second quality assessment, we check that the highest amplitude signals present in the vespagram align closely to the expected slowness found during beampacking, assuming that *pP* and *sP* phases travel at a similar slowness to the *P* arrival. Vespagrams lacking coherent arrivals both above the background noise level and at a consistent slowness will exhibit a greater standard deviation of their most coherent phases away from the expected slowness.

We implement this check by extracting the sample points (10 Hz sampling rate) on each vespagram (made up of beams stacked at 0.001 s/km slowness intervals) which possess an amplitude greater than 60 per cent of the maximum value within a time window (98 per cent of the modelled *P* to 102 per cent of the modelled *sP* arrival time) incorporating the modelled arrival times for *P*, *pP* and *sP*, whilst retaining their slowness and time information. In a coherent vespagram, these points should gather around key phase arrivals approximately with a slowness found by the beampacking process (see Section 2.4.1) if the phases are derived from the *P* wave and its coda. We apply the DBSCAN clustering algorithm (Ester *et al.* 1996) to identify significant groups of coherent points (coloured crosses in lower panel for each event on Fig. 8) and calculate the centres of the clusters (red points on Fig. 8). The centres are used to determine mean slowness across the arrival clusters, weighted according to the size of the cluster, and the standard deviation of the cluster centres. In order to continue through to the relocation stage, a vespagram needs to exhibit a mean cluster slowness within 0.006 s /km of the beampacking slowness and a cluster centre standard deviation of less than 0.0105 s /km.

Ad-hoc arrays which form vespagrams that display high amplitude phase arrivals located within 0.006 s /km of the expected *P* arrival slowness found via beampacking (see Section 2.4.1) will pass the quality check (Fig. 8a) and be automatically picked for *P*, *pP* and *sP* arrivals, if present, by the process described in Section 2.4.4. Fig. 8 also shows examples of *ad-hoc* array vespgrams which fail the quality check – due to the standard deviation of the cluster centres about the threshold (in b), a weighted mean slowness outside the bounds (in c) and due to both the standard deviation and weighted mean (in d).

After the cross-correlation and vespagram quality checks, the remaining *ad-hoc* arrays should have noisy traces removed to allow the cleanest beam to be stacked, and have demonstrated coherent vespagrams with respect to slowness. See Fig. S6 (Supporting Information) showing the mean percentage of arrays removed per magnitude due to the quality assessments used for the

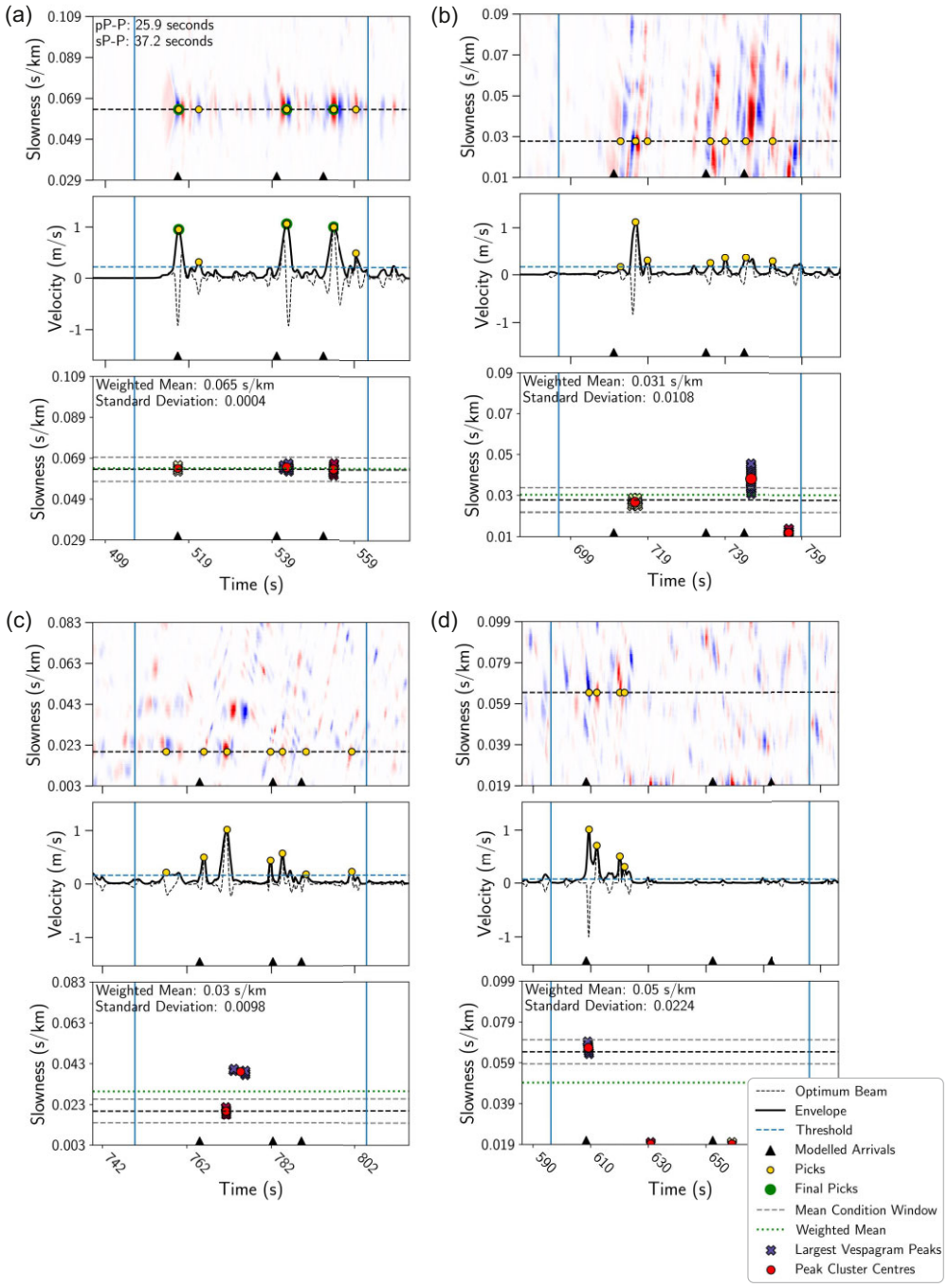

Figure 8. Four *ad-hoc* arrays from four different earthquakes demonstrating the determination of vespagram quality thresholds (see Section 2.4.3). Each set of three panels shows from top to bottom, the vespagram (see Section 2.4.2) with all picks in yellow (see Section 2.4.4), the optimum beam with picks and the corresponding DBSCAN vespagram quality test (see Section 2.4.3). The blue vertical lines indicate the time window used to assess data quality. *Ad-hoc* array (a) is from the m_b 6.2 event on 2010 May 23 at an epicentral distance of 48.99°. *Ad-hoc* array (b) is from the m_b 6.4 event on 2017 October 10 at an epicentral distance of 78.35 °. *Ad-hoc* array (c) is from the m_b 5.1 event on 2014 May 15 at an epicentral distance of 88.36°. *Ad-hoc* array (d) is from the m_b 4.9 event on 2006 June 7 at an epicentral distance of 63.27°.

Peruvian event catalogue defined in Section 2.1. For earthquakes with magnitudes below 4.7, the mean percentage of arrays removed is 86.4 per cent, indicating a very low success rate and confidence when our relocation approach is applied to events with magnitudes lower than 4.7. Above magnitude 4.7, there is – unsurprisingly – a negative correlation between earthquake magnitude and the mean percentage of arrays removed as higher magnitude earthquakes tend to generate larger amplitude, more coherent signals. The quality assessments enable the automated picking routine (see Section 2.4.4) a greater probability of success.

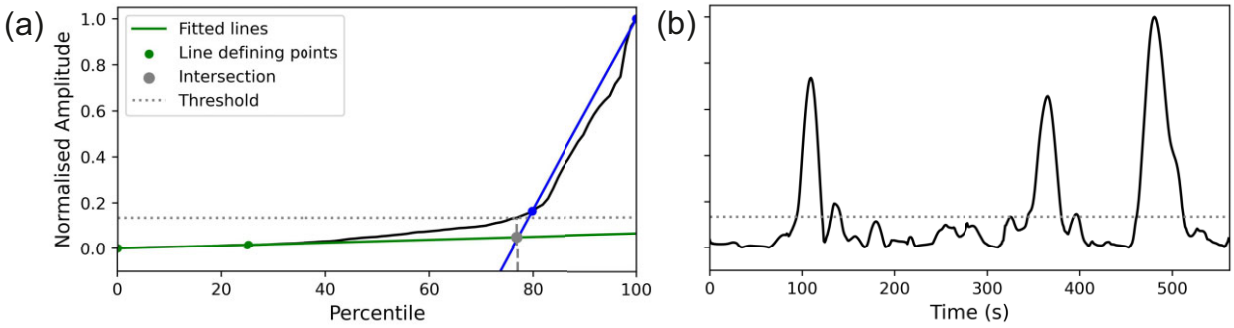

Figure 9. Example of the automatic picking threshold found for an *ad-hoc* array at an epicentral distance of 48.31° from the m_b 6.2 event on 2010 May 23. (a) Distribution of amplitude values for the *ad-hoc* array beam with respect to the percentile, the approximation of the beam with two lines, their intersection and the final threshold found. (b) Threshold relative to the phase weighted beam.

2.4.4 Automated picking routine

We take the *ad-hoc* arrays which have passed the vespagram quality check outlined in Section 2.4.2, and pick the *P*, *pP* and *sP* arrivals with an automated routine (Fig. 2). The picks found via the automatic picking routine subsequently have phases assigned to them during the phase identification stage (see Section 2.4.5), before the differential times between *pP–P* and *sP–P* are calculated to convert for depth (see Section 2.5). We describe the automated picking routine in this section.

The routine uses the envelope of the phase-weighted beam created at the best fitting slowness (see Section 2.4.1) – we shall call this beam, the optimum beam. The approach identifies peaks along the optimum beam with a significant prominence above a dynamic threshold, calculated from the distribution of the beam amplitudes. The use of a dynamic threshold, as opposed to a window based approach, decreases dependence upon the velocity model and the modelled phase arrivals, however the risk of extra and/or mis-identified picks increases. We handle this issue by applying a phase identification step, described in Section 2.4.5.

During the automated picking routine, the optimum phase weighted beam for the *ad-hoc* array is trimmed, using arrival times determined through the ak135 1D Earth model (Kennett *et al.* 1995), to only include the expected *P*, *pP* and *sP* phases. The envelope of the trimmed beam is calculated and peaks with a prominence exceeding 15 per cent of the maximum amplitude peak are identified.

The identified peaks are further filtered by a dynamic amplitude threshold, which is found using the distribution of amplitude in the trimmed envelope data. When the amplitudes of the data are plotted against the percentile, there is a rapid increase in the amplitudes associated with the higher percentiles of the data which correspond to the coherent phase arrivals (Fig. 9). We find the onset of the amplitude increase by approximating the pre- and post-increase slopes with lines and determining their intersect. The percentile associated with the intersect can thus be converted into its corresponding amplitude – the threshold amplitude (Fig. 9). Any peaks found to be higher in amplitude than this threshold will be preserved as potential picks for phase identification (see Section 2.4.5).

2.4.5 Phase identification

During the automated picking routine (see Section 2.4.4) issues can arise in instances where an expected phase lacks sufficient amplitude to be observable (allowing for phase misidentification) or more than three peaks are identified during the automatic picking routine (leading to ambiguity in phase identification). Here, we develop a phase identification routine (see Fig. 2 for placement of the routine in the overall approach, see Fig. 10 for the phase identification workflow) to identify picks which correspond to the expected phases, if one of the *P*, *pP* or *sP* phases are missing from the vespagram, the routine will only identify the phases present. Unfortunately, this process is reliant upon a reasonable initial event depth (within ± 40 km of the re-located depth) taken from the initial event catalogue (see Section 2.1), the velocity model and the resulting modelled arrivals.

Initially, the routine checks that the current set of picks are significantly greater in amplitude than the background noise of the data. We approximate the background noise amplitude by extracting 40 s of the optimum beam envelope recorded immediately before, yet not including the expected *P* wave arrival, and calculating the mean amplitude. For each pick, the ratio between the amplitude of the envelope at the pick and the calculated background noise must exceed 5 (following Florez & Prieto 2017) to be considered significant enough to be continued as a phase pick candidate.

The routine subsequently considers each remaining pick relative to one another, calculating the differential times between all the possible pairs of picks. *Ad-hoc* arrays with single picks are no longer considered at this point. Differential times between the pairs of picks are then compared with the 1-D modelled differential times for *pP–P* and *sP–P* determined using the ak135 velocity model (Kennett *et al.* 1995), and any pairs with a differential time within ±25 per cent of the modelled *pP–P* or *sP–P* differential times are taken forward as reasonable candidates.

For earthquakes at the shallow end of the depth range we consider, modelled differential times within ±25 per cent for a given pair will provide a very small time margin. To address this issue we replace the margins with constant values of 8.5 and 12.5 s when the 25 per cent margin becomes less than 8.5 s for *pP–P* and 12.5 s for *sP–P*, respectively. These constant margins are based upon the possible error in differential times assuming that the earthquake is within ± 40 km from the initial catalogue depth (see Fig. S7, Supporting Information).

At this stage, the routine has pairs of picks which have been identified as candidates for either the *pP–P* pairing or the *sP–P* pairing, which need to be reconciled. If there are only candidates for either the *pP–P* or *sP–P* pairing, the largest combined amplitude pair is selected. If there are candidates for both pairings, we start by

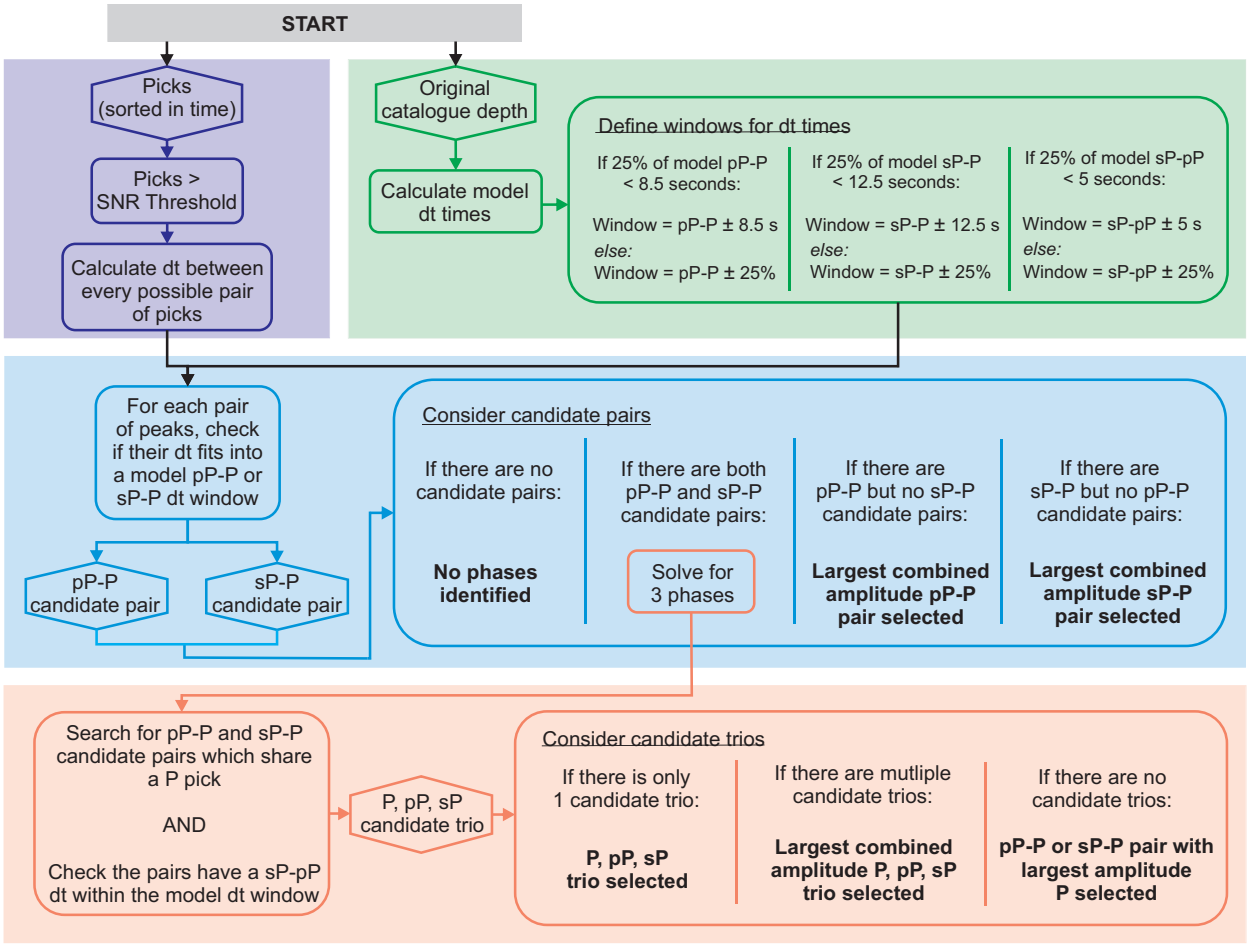

Figure 10. Phase identification workflow. Picks from the automatic picking routine are sorted into phases by comparing their differential times with the 1-D velocity modelled differential times for *pP–P*, *sP–P* and *sP–pP*. Hexagonal boxes indicate products from a step in the workflow, and bold text shows the final phase selections.

checking for a compatible set of *pP–P* and *sP–P* pairs by searching for matching *P* picks between the pairs, and for a reasonable separation in time for the associated *pP* and *sP* picks – a differential time within ±25 per cent (or 5 s, if ±25 per cent is less than 5 s) of the modelled *sP–pP* time. If only one complete *P*, *pP* and *sP* trio remains after this step, we select these as our final picks. If multiple trios remain, the complete set of picks with the largest combined amplitude is selected as the final picks. This assumes that the *P* arrival, and the depth phases, form the largest amplitude peaks. If there are candidates for both sets of pairs which cannot co-exist (i.e. their *P* arrivals do not match), the *P* candidate with the largest amplitude will be chosen preferentially and the associated depth phase selected. Note that the phase identification routine requires a *P* arrival to output final picks – a requirement which would exclude *ad-hoc* arrays that are nodal or near-nodel on the *P* wave radiation pattern.

Our process ensures that only good quality *ad-hoc* arrays with clear *P*, *pP* and/or *sP* arrivals are picked and identified. Finally we calculate the differential times between the final depth phases and their *P* arrival. We pass the *ad-hoc* array results through to the depth conversion stage (see Fig. 2), where both the *pP–P* and the *sP–P* times, if found, will be used to determine an event depth (see Section 2.5).

2.5 Depth conversion

After processing all of the *ad-hoc* arrays for a given earthquake, the algorithm considers the results from each *ad-hoc* array (i.e *pP–P* and *sP–P* differential times) relative to one another. The *ad-hoc* array outputs are post-processed to remove obvious outliers and provide final depth statistics (see Fig. 2).

To remove results from anomalous *ad-hoc* arrays, we calculate apparent depths for all of the *pP–P* and *sP–P* differential times (see Section 2.4.5) in order to directly compare *pP* and *sP* results and thus, create a larger population for identifying outliers. The depth conversion is a simple forward model. A range of test depths are defined from the initial catalogue depth (see Section 2.1) ± 40 km, with 0.1 km intervals. For the *ad-hoc* array in question, the differential traveltime for each test depth is forward modelled. The test depth with the smallest residual between the modelled and the determined differential times is adopted as the best-fitting depth for this *ad-hoc* array. This is conducted independently for the *pP* and *sP* results of each *ad-hoc* array initially to achieve the distance–depth population.

We apply a linear regression to the resulting distance-depth population, whereby *ad-hoc* array depths which exceed the median ± 1.3 of the standard deviation are removed from the data

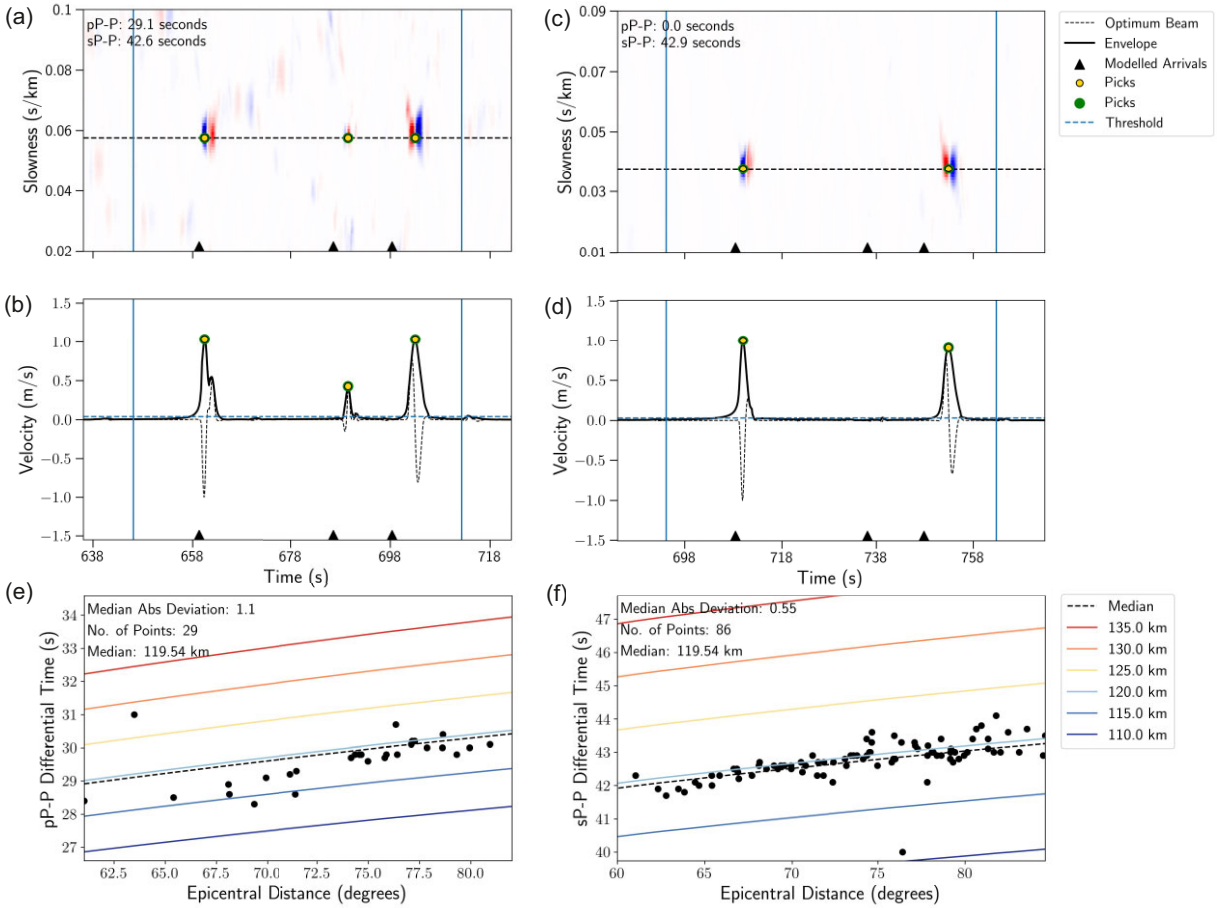

Figure 11. Example *ad-hoc* arrays, their automatic picks and differential times between phases for the M_w 5.5 event which occurred on 2008 December 4 in northern Chile, and plots illustrating all *ad-hoc* array differential times against epicentral distance to determine a final event depth. (a) and (b) are the vespagram and optimum beam, respectively, for an *ad-hoc* array at an epicentral distance of 69.9°, whilst (c) and d) are the vespagram and beam for an *ad-hoc* array at an epicentral distance of 78.4°. Blue vertical lines indicate the time window of data used for automatic picking. (e) and (f) show distance-differential time plots for *pP–P* and *sP–P* respectively. For this event the *sP* arrivals are clearly observed at each *ad-hoc* array, whilst the *pP* arrivals are significantly less apparent and smaller in amplitude. The differential times for *sP–P* seen in plot (f) are therefore more consistent with respect to epicentral distance than the *pP–P* times seen in (e), and notably weight the final hypocentral depth of 119.5 km.

set. These depths typically correspond to mis-picked and/or mis-identified phases, for the linear regression to be effective, we assume that there are more correct picks than mis-picks. We use the median as it is less susceptible to outlying data points. Remaining *ad-hoc* arrays are used in a second forward model designed to determine depth per *ad-hoc* array by minimizing the residual between the modelled differential times for both the *pP* and *sP* differential times. The median depth found from the *ad-hoc* array population using both the *pP* and *sP* differential times simultaneously provides the best indicator of the final earthquake hypocentre depth.

There is the option to use any 1-D velocity model for the final depth determination. Throughout the depth conversion for the Peruvian data (see Section 2.2), we use a regionally modified version of ak135 1-D velocity model (Kennett *et al.* 1995). To develop the model we take the 3-D velocity cube for the region determined by Lim *et al.* (2018), extract the velocities above the location of slab indicated by the Slab2 model (Hayes *et al.* 2018) and average the velocities per depth interval. We then replace the upper portion of the 1-D ak135 velocity model with the values determined from the regional 3-D velocity cube. Alternatively, there is flexibility to parse the cleaned differential *pP–P* and *sP–P* times into an alternate depth inversion algorithm, such as ISCloc developed by the ISC (Bondár & Storchak 2011).

3 VALIDATION

3.1 Single event

We test the relocation algorithm outlined in Section 2 on a magnitude 5.5 event from northern Chile which occurred on the 2008 December 4. This event is catalogued with a depth of 108.8 km by the ISC, and has previously been updated to a depth of 117 km by Florez & Prieto (2017) using 12 fixed medium-aperture arrays and a *pP* depth phase-based methodology in conjunction with the ak135 1-D velocity model (Kennett *et al.* 1995). Using the same velocity model, and our adaptive *ad-hoc* array approach, we find a depth of 119.5 km from 86 *ad-hoc* arrays (Fig. 11). The *ad-hoc* arrays demonstrate a strong *sP* arrival and, if present, a substantially weaker *pP* arrival, which has allowed the *sP–P* differential times to significantly weight the final depth determined. This likely accounts

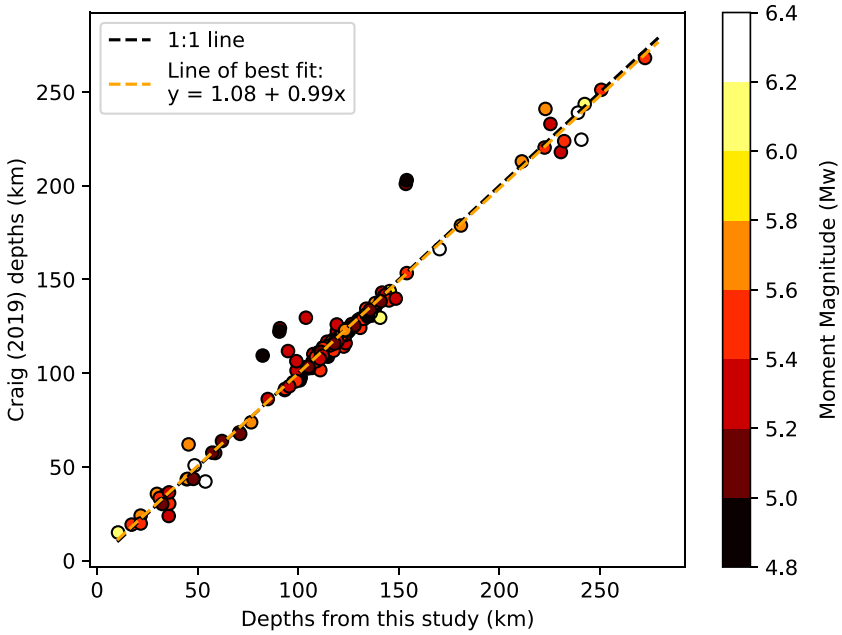

Figure 12. Depths of northern Chilean earthquakes as found by Craig (2019) against the depths found in this study.

for the slight difference to the depth determined by Florez & Prieto (2017), whose approach only used *pP–P* delay times.

3.2 Regional catalogue comparison

To further assess the performance of our new earthquake relocation algorithm, we relocate the same earthquakes as presented in the regional catalogue of Craig (2019) from northern Chile. Craig (2019) stacked a global teleseismic data set per candidate depth to identify the optimal depth to beamform depth phases, and hence determine hypocentre depth. As both studies use global teleseismic data sets and fix the latitude and longitude coordinates of the hypocentre during relocation, the results should be comparable. One key difference between this study and the study of Craig (2019) is the automation – this study uses a fully automated methodology, whilst Craig (2019) take a semi-automated approach, including automated stacking and phase picking using kurtosis, manual choices concerning the number of depth phases to pick, and by-hand quality control checks.

The compared earthquakes range from moment magnitudes of 4.8–6.4, and are found between 10 and 280 km depths (Fig. 12). To ensure a thorough comparison, we have applied the same velocity model as Craig (2019) for the depth relocation step of the algorithm (see Section 2.5). Our relocation depths are in good agreement, demonstrating a mean difference in depth of 4.13 km and a strong alignment of the line of best fit to the the 1:1 ratio. There are a number of events with differing results, those with larger residuals are towards the lower end of the magnitude scale. We show two example events with differing depths in Supporting Information (Fig. S8), which we believe are relocated well with our new approach, despite a disagreement in depth. These results demonstrate that our fully automated, computationally efficient relocation approach for northern Chile is performing well compared to previous semi-automated and manually quality controlled routine. The catalogue comparison also demonstrates that our methodology can relocate events which are shallower than intermediate-depth earthquakes (<40 km). We have previously tested this with a moment magnitude 5.3 event in Algeria, with a depth of 31 km (Wimpenny *et al.* 2023). A map and two cross-sections of the Chilean catalogue are in Supporting Information, see Fig. S9.

4 REGIONAL APPLICATION—PERUVIAN FLAT SLAB

The Peruvian flat slab region is a zone of relatively shallow subduction located directly underneath Peru. It extends approximately 1600 km NW-SE and 300 km downdip, plateauing at around 100 km depth (Hayes *et al.* 2018) before subducting further into the mantle at a 30° dip (Portner & Hayes 2018). Its location has been recently refined and updated through integrating seismicity with tomography for the Slab2 model (Portner & Hayes 2018) – a global data set of depth data for subducting slabs. However there is currently no regional intermediate-depth earthquake catalogue which incorporates the entire flat slab. A wholesale catalogue for the flat slab is likely to prove useful when it comes to trying to establish controls upon flat slab formation and intermediate-earthquake distribution, in addition to questions related to the slab geometry and structure.

We present results from a magnitude 4.7 event in Fig. 13 to demonstrate the ability of the algorithm to successfully relocate small magnitude earthquakes and the potential to adapt the algorithm to push the lower magnitude bound further. The event has been relocated from a depth of 60.8 km provided by the ISC to 46.6 km using our approach. Notably there is an extra phase in Fig. 13(a) and (b) between the *P* and *pP* arrivals, also seen on several other *ad-hoc* arrays' data, which may be a *pmP* arrival. A *pmP* wave is a near-source Moho reflection which can be used relative to the *pP* arrival time to determine crustal thickness (McGlashan *et al.* 2008). The detection of such phases highlights the potential for the relocation algorithm presented in this paper to be adapted to boost the signal-to-noise ratios of alternative

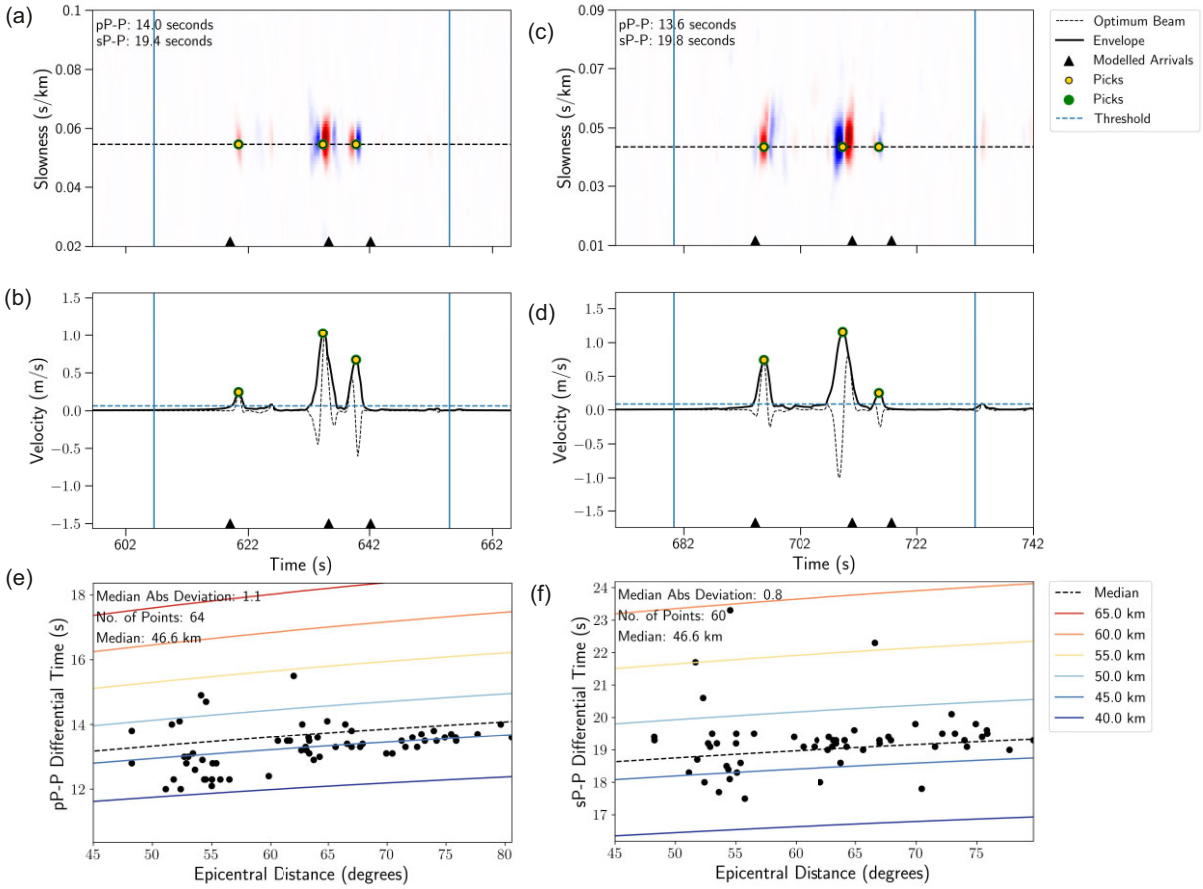

Figure 13. Example *ad-hoc* arrays, their automatic picks and differential times between phases for the m_b 4.7 event which occurred on 2022 May 27 in Peru, and plots illustrating all *ad-hoc* array differential times against epicentral distance to determine a final event depth. (a) and (b) are the vespagram and optimum beam respectively for an *ad-hoc* array at an epicentral distance of 62.8°, whilst (c) and (d) are the vespagram and beam for an *ad-hoc* array at an epicentral distance of 74.9°. Blue vertical lines indicate the time window of data used for automatic picking. (e) and (f) Distance-differential time plots for *pP–P* and *sP–P*, respectively. Plots (e) and (f) show that depth phase picks can be difficult to pick well automatically and gather consistent differential times, however a large number of data points (124) helps to combat the poorer picks.

small amplitude arrivals, and automatically detect them for further analysis.

Additionally in Fig. 14 we demonstrate the outputs of the m_b 6.2, 2010 May 23 event. The vespagrams are from *ad-hoc* arrays located at 48.3° and 64.8° from the epicentre, and the new depth determined is 102.8 km from an initial depth of 99.6 km from the ISC. Note that with mean uncertainties of approximately 3 km (see Section 4.2), these depths are not significantly different.

4.1 Determining a lower magnitude limit

We determine an appropriate lower magnitude threshold for our approach using the Peruvian relocation results. The event catalogue tested contains earthquakes from m_b 3.0 to 6.5 from post-1995 taken from the ISC (see Section 2.1). By considering the number of relocated events relative to the total number of events in the catalogue, and the number of *ad-hoc* arrays with at least either a *pP–P* or *sP–P* differential time relative to the total number of *ad-hoc* arrays made per magnitude. We find a lower threshold of m_b 4.7, where the algorithm ceases to obtain consistent results due to a significant reduction in the number of high-quality *ad-hoc* arrays (see Fig. 15). Whilst depth phases can be found for smaller events, close inspection of the resulting vespagrams indicates that the true success rate of our routine rapidly decreases below m_b 4.7 – we find that coherent noise is typically picked on the low number of *ad-hoc* arrays remaining after data quality checks, which skews how successful these events appear. We therefore suggest m_b 4.7 as an operational magnitude limit, and recommend inspection of formative lower magnitude events.

4.2 Assessing error

To provide a quantitative measure of the uncertainty present in the *pP–P* and *sP–P* differential times, which are later converted to depth, we jack-knife the traces of each *ad-hoc* array used to determine the final depth relocation of each earthquake.

For each *ad-hoc* array, we randomly remove one trace and pass the remaining traces through the processing and analysis loop. This tests the dependence of the *ad-hoc* array's results upon a single trace. Since the minimum number of traces permitted in an *ad-hoc* array is 8 (see Section 2.4.3), we jack-knife the traces and run the loop eight times, before running the loop once more with all of the traces included to give a total of nine runs per *ad-hoc* array. The same trace is not removed twice, therefore each *ad-hoc* array can have a maximum of 9 *pP-P* and 9 *sP-P* times, and thus a maximum of 18 associated depths.

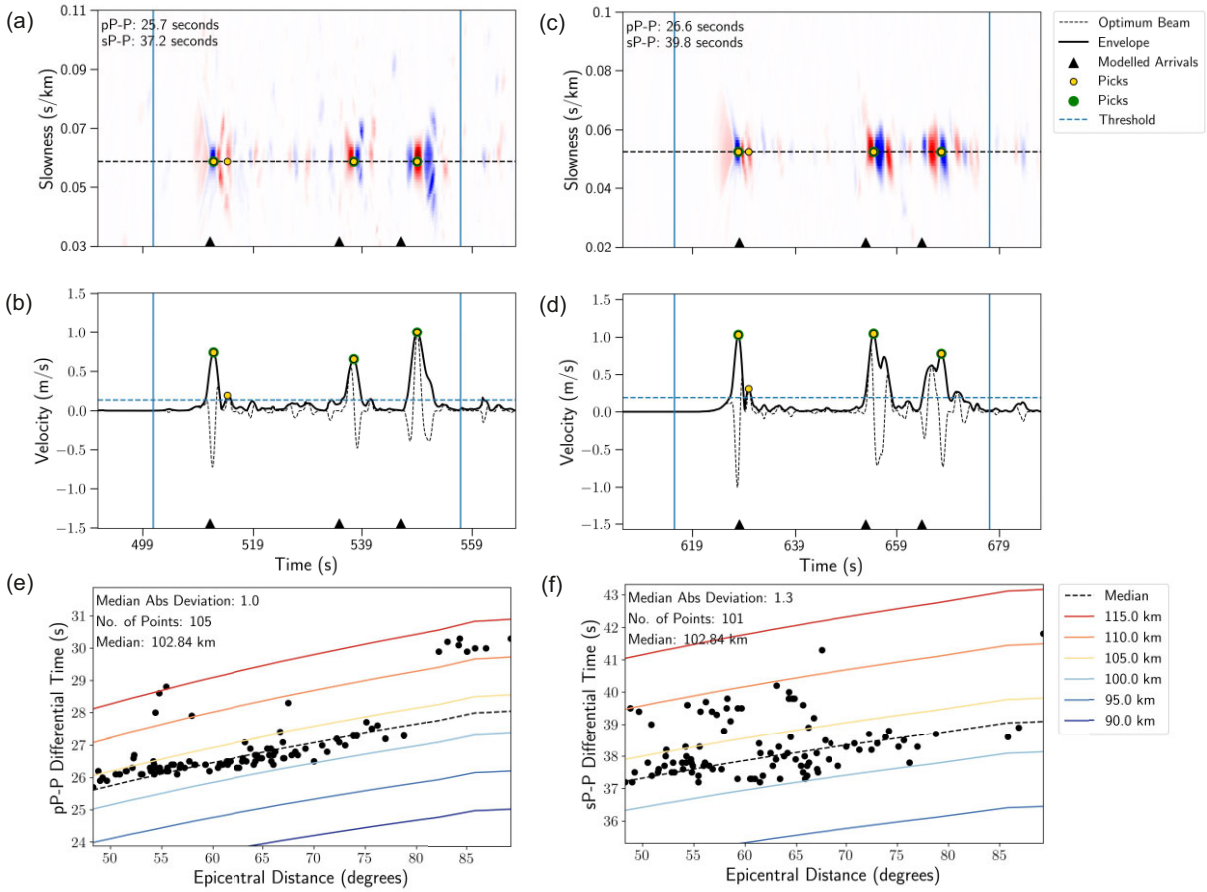

Figure 14. Example *ad-hoc* arrays, their automatic picks and differential times between phases for the m_b 6.2 event which occurred on 2010 May 23 in Peru, and plots illustrating all *ad-hoc* array differential times against epicentral distance to determine a final event depth. (a) and (b) are the vespagram and optimum beam respectively for an *ad-hoc* array at an epicentral distance of 48.3°, whilst (c) and (d) are the vespagram and beam for an *ad-hoc* array at an epicentral distance of 64.8°. Blue vertical lines indicate the time window of data used for automatic picking. (e) and (f) show distance-differential time plots for *pP–P* and *sP–P*, respectively. On plot (e) the deeper picks determined from *ad-hoc* arrays at epicentral distances over 80° appear anomalous, these are located in Europe where perhaps the velocity model is not fitting the ray path well. Plot (f) shows that for this event *sP* picks can be more difficult to pick well automatically and gather consistent differential times. The cluster of *ad-hoc* arrays near a depth of 108 km occur due to a slight mis-pick as demonstrated by *sP* picks seen in (c) and (d).

After jack-knifing each *ad-hoc* array for a single earthquake, we post-process the results identically to the usual relocation routine and calculate the median absolute deviation of the remaining *ad-hoc* array distance–depth data points to assess how the differential times uncertainty translates to error in depth. This is repeated for every earthquake in the relocated catalogue, ensuring an event-specific uncertainty is determined for each relocated earthquake depth. We also preferentially use the median event depth found from the jack-knifed *ad-hoc* arrays as our final hypocentral depth – the larger number of data points typically provides a more precise depth and this value relates directly to the errors calculated.

For our regional catalogue, we remove events with zero error, thus removing events with their depths determined from a single *ad-hoc* array. We also remove events with an exact 40 km depth change from the original ISC catalogue, as these indicate events which cannot be relocated by our approach due to the ± 40 km test depth limit used during depth conversion. We additionally limit the events to between m_b 4.7–6.5. The remaining events demonstrate errors ranging between 23.10 and 0.05 km with a mean uncertainty of 3.13 km. For our final regional catalogue we choose to not include events providing errors greater than 20 km, the errors for the final catalogue vary between 0.05 and 18.40 km, with a mean uncertainty of 3.05 km – less than 5 per cent of the events have errors >10 km. These uncertainties are illustrated as error bars on the Peruvian catalogue shown in Fig. 16. The mean difference between the final catalogue depths and the initial ISC depths is 4.18 km, however the use of different velocity models will systematically factor into this variation – see Fig. S10 in the Supporting Information.

4.3 Relocated Peruvian catalogue

The final Peruvian catalogue demonstrates the automatic relocation of 620 earthquakes, and shows three broad zones of seismicity (Fig. 16a) approximately between latitudes 1–7°S, 7–13°S and 13–19°S — the northern and southern most zones are located over the areas where the flat slab portion of the Nazca plate is transitioning into a steeper slab dip. The seismicity between 7–13°S includes the Pucallpa Nest, which is thought to be related to both the Mendaña Fracture Zone and a local slab sag (Wagner & Okal 2019). The three cross-sections (Figs 16b–d) aim to target these zones.

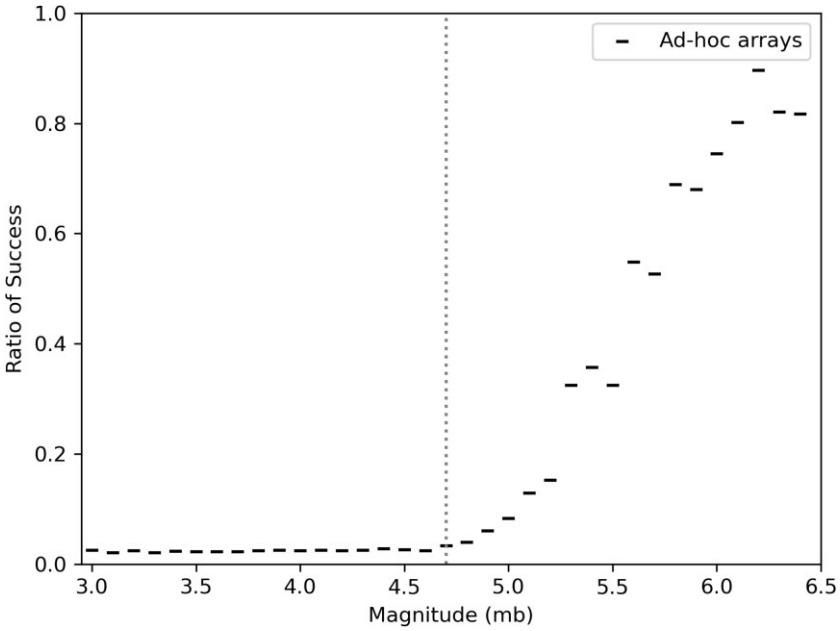

Figure 15. Determining the lower magnitude limit for our approach using the Peruvian catalogue containing 8796 earthquakes from m_b 3.0 to 6.5 which have occurred post-1995, taken from the ISC. Ratio of successful versus failed relocations for total *ad-hoc* arrays per 0.1 moment magnitude. The dashed line highlights our m_b 4.7 limit.

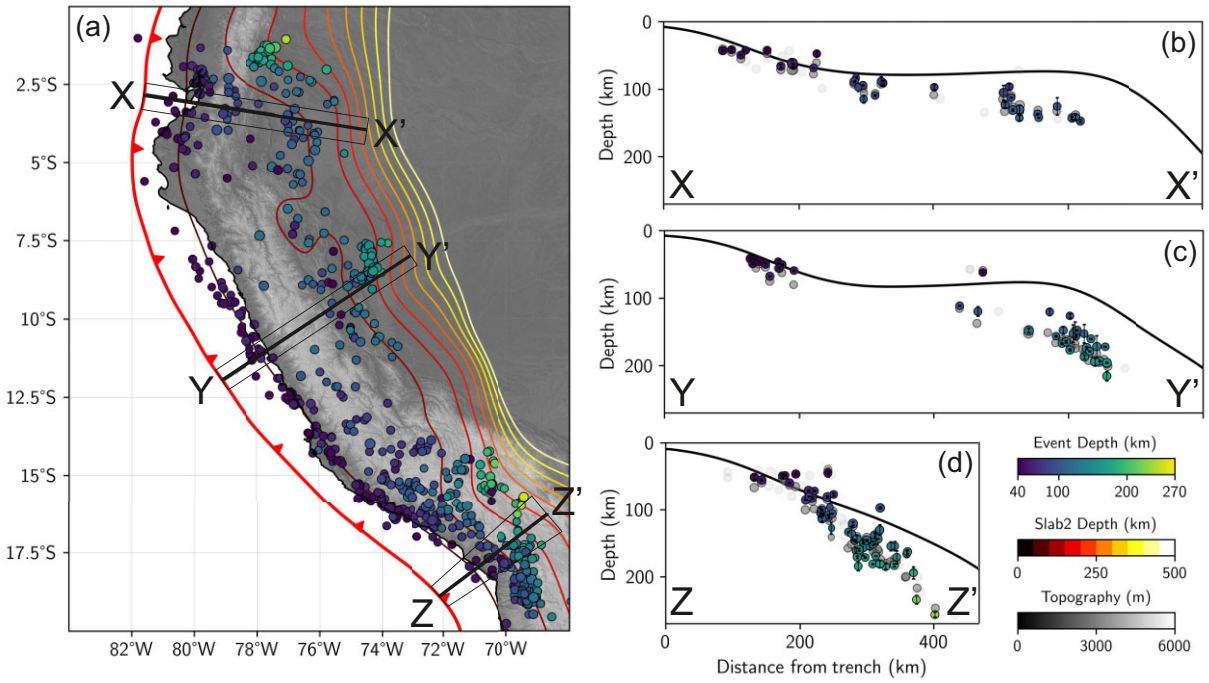

Figure 16. Peruvian flat slab catalogue with error bars determined though jack-knifing the *ad-hoc* arrays. The figure shows events with magnitudes between m_b 4.7–6.5, and have final relocated depths between 40–350 km with errors of less than 20 km. (a) Map of Peru, with the relocated hypocentres, example cross-section locations and Slab2 contours plotted (Hayes *et al.* 2018). (b)–(d) Show the example cross-sections with our relocated hypocentral depths in colour with their error bars, the original ISC hypocentres which we relocated in dark grey and ISC hypocentres which were not relocated by our approach in pale grey. All plotted hypocentres are scaled in size by magnitude.

These profiles (Figs 16b and c) demonstrate the flat slab, with intraslab events occurring at the initial bend into the flat slab configuration approximately 100–300 km from the trench, and additionally when the slab bends again into the mantle between 450–750 km from the trench, with a largely aseismic stretch between the two bends. This observation supports the link between flexural bending of the downgoing slab and the occurrence of intermediate-depth earthquakes due to the resultant intraslab deformation (Sandiford *et al.* 2019). Fig. 16(d) also looks to have two layers of seismicity within the Pucallpa Nest, approximately 600 km from the trench. This could indicate the presence of a double seismogenic zone in central Peru, however further analysis

would be required to determine if the apparent layering is a real feature.

Fig. 16(d) demonstrates the steeper slab dip which the flat slab transitions into north and south of Peru. Whilst the section does capture events occurring at variable slab dips in and out of the projection plane – note the two events at approximately 375–400 km from the trench at depths of 230–260 km – it is apparent that a new regional slab top deviating from Slab2 (Hayes *et al.* 2018) may be needed for the Peruvian portion of the Nazca plate. The tailored quantitative errors for each event determined from jack-knifing our *ad-hoc* arrays will help to inform future interpretations of the final catalogue.

5 LIMITATIONS

5.1 Assumed point source

For a hypocentral depth to be relocated, there is an automatic assumption that the seismic signal is emitted from a discrete spatial point. In reality whilst this can be a sound assumption for smaller magnitude events, larger earthquakes will likely have spatiotemporal evolution of their ruptures and focal mechanisms. For example, the M_w 8.0 intraslab event which occurred in Peru on the 2019 May 26 demonstrated multiple rupture episodes (Hu *et al.* 2021) with two large slip areas approximately 120 km apart (Liu & Yao 2020). Complex rupture propagations, and the spatial areas they cover, are not taken into consideration whilst relocating the earthquake depth. We limit the magnitude of the earthquake events we consider to $m_b < 6.5$ in order to avoid ruptures that appear complex at the frequencies used in our approach, and to assist the assumption of a simple point source.

5.2 Velocity model

Currently, the automated routine we have developed uses a 1-D global velocity model modified to reflect regional variation in lithosphere velocity structure to predict phase arrivals, and convert the differential times into depth. The 1-D velocity model does not take into account the near-source variance in crustal structure and topography, the depth phases are experiencing with respect to receiver azimuth. To address this limitation we would need to incorporate a 3-D velocity structure and ray tracing into the relocation algorithm.

However, the algorithm possesses the flexibility to outsource the depth conversion to an alternative inversion algorithm, which may use a 3-D velocity structure during depth relocation – the phase picking routine is independent of the predicted phase arrival times and the phase identification routine has a modest margin of error built in to account for ray path errors. Additionally, the greater the epicentral distance of the station (i.e. further than 30°), the closer the depth phase bounce points exist to the event epicentre. This limits the velocity variations the depth phases experience relative to one another. Most teleseismic stations, and hence the *ad-hoc* arrays, are situated more than 30° from the event epicentre.

5.3 Shallow events

The ability to relocate shallow earthquakes depends upon whether there is sufficient separation between the direct arrival and its corresponding depth phases to allow the identification of distinct arrivals, which in turn is dependent upon the source duration (which broadly scales with earthquake magnitude). If the source duration of a shallow earthquake is small, the likelihood that the phases will separate enough to allow relocation to occur increases.

The relocation algorithm presented here has been designed to relocate earthquakes which occur between 40 and 350 km depth, however, we have observed robust relocations for depths sub-40 km. Whilst earthquakes with short source durations and depths down to ∼15 km have been relocated by the algorithm as it currently exists, some adaptations would be necessary to increase confidence in the phase identification routine for events sub-25 km deep.

5.4 Focal mechanism

In some cases the combination of station azimuth with take-off angle results in a *P* wave ray path where the pierce point aligns with one of the event's nodal planes. When this happens there will be no detectable *P* arrival at the station due to the *P* wave radiation pattern. Without a *P* arrival, the relocation algorithm presented here cannot be used. *Ad-hoc* arrays containing data without a *P* wave arrival will be discarded by the phase identification routine (see Section 2.4.5), thus reducing the pool of *ad-hoc* arrays used to determine event depth.

Similarly, the detection of each individual depth phase depends upon the phase having a detectable amplitude, and is therefore limited in cases where the pierce point for that phase intersects with the radiation pattern nodal plane. Hence, even when *P* is clearly detectable, one or both of *pP* and *sP* may have small amplitudes, and be undetectable. This is the principal contributor to the complexity in our phase identification routine.

5.5 Station density

For a robust depth determination using our relocation algorithm, the formation of multiple *ad-hoc* arrays is required. For multiple *ad-hoc* arrays to be formed, we need a dense distribution of seismic stations, ideally spanning a range of distances and azimuths. Whilst the growth of seismic network coverage means future events will have a wealth of data recorded by the expanding open access seismic networks, historic events sometimes lack coverage. Events occurring pre-2000 struggle for data with a great enough station density for *ad-hoc* array formation under the criteria outlined in Section 2.3. The exceptions to the rule are events from the 1990s which contain dense, targeted station networks within teleseismic distances, such as the seismometers associated with the Southern California Earthquake Data Centre, or dense networks installed as part of temporary regional deployments. Yet even these events will suffer from a lack a backazimuthal variation if, for example, the nodal plane of the event focal mechanism aligned with the few existing *ad-hoc* arrays (see Section 5.4). Despite the occasional dense network available during the 1990s, older events are likely to suffer from the low-density distribution of seismic data. The approach is unlikely to work pre-1990s due to a lack of global data.

5.6 Automation

We have consciously set high-quality control measures in order to build confidence in the automated results. Consequently, clean coherent data may occasionally be discarded alongside poorer quality data. Equally, despite the high-quality control measures, the occasional poor-quality data *ad-hoc* array, or mis-identified phase,

may proceed through to the depth determination steps. We aim to capture the uncertainty of the new event depths based upon poorer quality data within the jack-knifing error estimations (see Section 4.2).

5.7 Maximum catalogue depth error

The phase identification routine and the depth inversion are designed to accommodate a maximum of 40 km error in the initial catalogue depth. The phase identification routine relies upon the predicted phase arrivals plus margins of error calculated from a potential 40 km error in the initial catalogue depth, and the forward modelled test depths are limited to ±40 km of the initial catalogue depth. Any events which require an updated hypocentre depth that is greater than 40 km from the initial depth catalogue will not be correctly relocated, and hence would be excluded from a catalogue determined using our routine.

We use the ISC event catalogue as our initial catalogue as we expect that the event hypocentres they calculate are within 40 km of the depths we calculate using our algorithm, although we acknowledge that in rare cases, this may not be the case (e.g. Craig *et al.* 2023).

6 CONCLUSION

In this study, we present a fully automated, dynamic approach to constrain the depths of intermediate-depth earthquakes using depth phases. Depth phases are difficult to detect on single station seismic data, therefore we leverage the increasingly available global seismic data to construct adaptable *ad-hoc* arrays and apply array processing techniques, in order to significantly boost the detectability of both *pP* and *sP*. We use the differential times between the depth phases and their direct *P* arrival in conjunction with an appropriate 1-D velocity model to determine hypocentral depth. Using this approach we are able to reliably generate regional catalogues containing events between m_b 4.7 and 6.5, and between depths of 40–350 km. We show regional catalogue results for the northern Chile and the Peruvian flat slab sections of the subducting Nazca plate, with strong agreement between our depths for northern Chile and those found by Craig (2019).

ACKNOWLEDGMENTS

AB was supported by the Leeds-York-Hull Natural Environment Research Council (NERC) Doctoral Training Partnership (DTP) Panorama under grant NE/S007458/1. TJC was supported in this work by the Royal Society under URF\R1\180088, URF\R\231019 and RF\ERE\210041, and also through COMET, which is the NERC Centre for the Observation and Modelling of Earthquakes, Volcanoes and Tectonics, a partnership between UK Universities and the British Geological Survey. TJC and SR were also partly supported by the Leverhulme Trust through Research Grant RPG-2021-336. Much of this work was undertaken on ARC4, part of the High Performance Computing facilities at the University of Leeds, UK and using the Obspy seismology toolbox for Python (Beyreuther *et al.* 2010). We thank Tom Garth and Ryan Gallacher for useful discussions on earthquake location, and we thank the editor and two anonymous reviewers for their comments, which have helped improve the manuscript.

SUPPORTING INFORMATION

Supplementary data are available at *GJIRAS* online.

Figure S1 Plot showing the mean number of phases (*P*, *pP* or *sP*) found per moment magnitude whilst applying five different bandpass filters for three seismic data types – displacement, velocity and acceleration.
Figure S2 Plot showing the mean number of phases (*P*, *pP* or *sP*) found per depth whilst applying a 1–10 s bandpass filter for three seismic data types – displacement, velocity and acceleration.
Figure S3 Plots showing the difference between the plane and curved wavefront time-shifts required to beamform a theoretical station for *P*, *pP* and *sP* arrivals using the ak135 velocity model. The theoretical station is 278 km away from the beamforming coordinates at approximately 045° bearing. A range of source depths from 40 to 360 km are tested using a backazimuth of 180°. All three phases are calculated to have less than 0.2 s difference between the plane and curved wavefront time-shifts which significantly decreases with epicentral distance. Plots created using software from Ward *et al.* (2023).
Figure S4 Comparison grid of *P* arrival phase-weighted beams (power of 4) demonstrating the variation in the amplitude, and thus coherence, as the backazimuth and slowness values grade from those found by the geodetic calculations (red box) to those found by beampacking (green box). θ represents backazimuth and u represents slowness. Example is from an *ad-hoc* array located 57.9° from the 2010 May 23, m_b 6.2 earthquake.
Figure S5 Cross correlation results for ad-hoc arrays located at (a) 83.2° and (b) 83.1° epicentral distances from the 23rd May 2010, m_b 6.2 earthquake. (a) demonstrates an array where no traces fail the cross correlation quality control parameters, whilst (b) shows an *ad-hoc* array where the example trace fails to meet the specifications and is removed. The updated beam subsequently reflects an increased P arrival amplitude.
Figure S6 Mean percentage of arrays removed by the two data quality assessments - cross-correlation and vespagram based – per magnitude (m_b) of earthquake in the Peruvian event catalogue defined in Section 2.1. The grey dashed line indicates where 50% of arrays are removed by the quality assessments, and the grey dotted line highlights the onset of the negative correlation between magnitude and percentage of arrays removed, occurring at approx. m_b 4.7.
Figure S7 Plot illustrating the maximum differential times between the given phases for a 40 km deep source, assuming a depth error of 40 km. This is to determine reasonable fixed time/error margins during the phase identification routine for shallow earthquakes. Deeper earthquakes use a 25 per cent error margin during the phase identification routine.
Figure S8 Example *ad-hoc* arrays from northern Chile for two events with differing relocated depths to those found by Craig (2019). An M_w 6.4 event from 1999 September 15 with a hypocentre found to be 16.1 km deeper than Craig (2019) – vespagram (a) and optimum beam (b) for an *ad-hoc* array at an epicentral distance of 71.9°, and *pP–P* differential time plot (c). An M_w 5.3 event from 2001 May 24 with a 12.5 km deeper depth found by this study – vespagram (a) and optimum beam (b) for an *ad-hoc* array at an epicentral distance of 70.5°, and *pP–P* differential time plot (c).
Figure S9 Northern Chile catalogue with error bars determined though jack-knifing the *ad-hoc* arrays. The figure shows events with magnitudes between m_b 4.7–6.5, and have final relocated depths between 40–350 km with errors of less than 20 km. (a) Map of northern

Chile, with the relocated hypocentres, example cross-section locations and Slab2 contours plotted (Hayes *et al.* 2018). (b) and (c) Show the example cross-sections with our relocated hypocentral depths in colour with their error bars, the original ISC hypocentres which we relocated in dark grey and ISC hypocentres which were not relocated by our approach in pale grey. All plotted hypocentres are scaled in size by magnitude.

Figure S10 Histogram showing the difference in depths between the initial ISC event catalogue and the final Peruvian catalogue determined during this study.

Please note: Oxford University Press is not responsible for the content or functionality of any supporting materials supplied by the authors. Any queries (other than missing material) should be directed to the corresponding author for the paper.

DATA AVAILABILITY

All seismic data used in this study are openly available from BGR at http://eida.bgr.de, ETH at http://eida.ethz.ch, GEONET at http://service.geonet.org.nz, GFZ at http://geofon.gfz-potsdam.de, ICGC at http://ws.icgc.cat, INGV at http://webservices.ingv.it, IPGP at http://ws.ipgp.fr, IRIS at http://service.iris.edu, KNMI at http://rdsa.knmi.nl, LMU at http://erde.geophysik.uni-muenchen.de, NIEP at http://eida-sc3.infp.ro, NOA at http://eida.gein.noa.gr, ORFEUS at http://www.orfeus-eu.org, RESIF at http://ws.resif.fr, SCEDC at http://service.scedc.caltech.edu, TEXNET at http://rtserve.beg.utexas.edu, UIB-NORSAR at http://eida.geo.uib.no and USP at http://sismo.iag.usp.br. A full list of seismic networks used, and their DOIs, is provided in the Supporting Information. Final event catalogues for Peru and northern Chile using their regional 1-D velocity models are provided in the Supporting Information. Code is available on request from the authors.

REFERENCES

Abe, K., 1972. Mechanics and tectonic implications of the 1966 and 1970 Peru earthquakes, *Phys. Earth planet. Inter.,* **5**(C), 367–379.

Beck, S., Barrientos, S., Kausel, E. & Reyes, M., 1998. Source characteristics of historic earthquakes along the central Chile subduction zone, *J. South Am. Earth Sci.,* **11**(2), 115–129.

Beyreuther, M., Barsch, R., Krischer, L., Megies, T., Behr, Y. & Wassermann, J., 2010. ObsPy: a python toolbox for seismology, *Seismol. Res. Lett.,* **81**(3), 530–533.

Bondár, I. & Storchak, D., 2011. Improved location procedures at the International Seismological Centre, *Geophys. J. Int.,* **186**(3), 1220–1244.

Craig, T. & Hull, A., 2024. Extensional failure at the tip of a weak slab under slab pull–the 2023 Mw 6.4 Zacualpa, Guatemala, earthquake, *Seismica,* **3**(1), doi:10.26443/seismica.v3i1.1190.

Craig, T.J., 2019. Accurate depth determination for moderate-magnitude earthquakes using global teleseismic data, *J. geophys. Res.: Solid Earth,* **124**(2), 1759–1780.

Craig, T.J. & Heyburn, R., 2015. An enigmatic earthquake in the continental mantle lithosphere of stable North America, *Earth planet. Sci. Lett.,* **425**(2), 12–23.

Craig, T.J., Jackson, J.A., Priestley, K. & M C Kenzie, D., 2011. Earthquake distribution patterns in Africa: their relationship to variations in lithospheric and geological structure, and their rheological implications, *Geophys. J. Int,* **185,** 403–434.

Craig, T.J., Jackson, J., Priestley, K. & Ekström, G., 2023. A Cautionary Tale: examples of the mis-location of small earthquakes beneath the Tibetan plateau by routine approaches, *Geophys. J. Int.,* **233**(3), 2021–2038.

Devlin, S., Isacks, B.L., Pritchard, M.E., Barnhart, W.D. & Lohman, R.B., 2012. Depths and focal mechanisms of crustal earthquakes in the central Andes determined from teleseismic waveform analysis and InSAR, *Tectonics,* **31**(2), doi:10.1029/2011TC002914.

Dziewonski, A.M., Chou, T.A. & Woodhouse, J.H., 1981. Determination of earthquake source parameters from waveform data for studies of global and regional seismicity., *J. geophys. Res.,* **86**(B4), 2825–2852.

Ekström, G., Nettles, M. & Dziewoński, A.M., 2012. The global CMT project 2004-2010: Centroid-moment tensors for 13,017 earthquakes, *Phys. Earth planet. Inter.,* **200-201,** 1–9.

Engdahl, E., Van Der Hilst, R. & Buland, R., 1998. Global teleseismic earthquake relocation with improved travel times and procedures for depth determination, *Bull. seism. Soc. Am.,* **88**(3), 722–743.

Ester, M., Kriegel, H.-P., Sander, J. & Xu, X., 1996. A density-based algorithm for discovering clusters in large spatial databases with noise, in *Proceedings of the 2nd International Conference on Knowledge Discovery and Data Mining,* pp. 226–231, Edited by Simoudis, E., Han, J., & Fayyad, U., AAAI Press, Portland, Oregon.

Fang, H. & Van Der Hilst, R.D., 2019. Earthquake depth phase extraction with p wave autocorrelation provides insight into mechanisms of intermediate-depth earthquakes, *Geophys. Res. Lett.,* **46**(24), 14440–14449.

Ferrand, T.P. *et al.*, 2017. Dehydration-driven stress transfer triggers intermediate-depth earthquakes, *Nat. Commun.,* **8,** doi:10.1038/ncomms15247.

Florez, M.A. & Prieto, G.A., 2017. Precise relative earthquake depth determination using array processing techniques, *J. geophys. Res.: Solid Earth,* **122**(6), 4559–4571.

Frohlich, C., 2006. *Deep Earthquakes,* Cambridge University Press.

Hacker, B.R., Peacock, S.M., Abers, G.A. & Holloway, S.D., 2003. Subduction factory 2. Are intermediate-depth earthquakes in subducting slabs linked to metamorphic dehydration reactions?, *J. geophys. Res.: Solid Earth,* **108**(B), doi:10.1029/2001JB001129.

Hayes, G.P., Moore, G.L., Portner, D.E., Hearne, M., Flamme, H., Furtney, M. & Smoczyk, G.M., 2018. Slab2, a comprehensive subduction zone geometry model, *Science,* **362**(6410), 58–61.

Heyburn, R. & Bowers, D., 2008. Earthquake depth estimation using the F trace and associated probability, *Bull. seism. Soc. Am.,* **98**(1), 18–35.

Hosseinzadehsabeti, E., Ferré, E.C., Persaud, P., Fabbri, O. & Geissman, J.W., 2021. The rupture mechanisms of intraslab earthquakes: a multiscale review and re-evaluation, **221,** doi:10.1016/j.earscirev.2021.103782.

Hu, Y., Yagi, Y., Okuwaki, R. & Shimizu, K., 2021. Back-propagating rupture evolution within a curved slab during the 2019 Mw8.0 Peru intraslab earthquake, *Geophys. J. Int.,* **227,** 1602–1611.

Kennett, B.L., Engdahl, E.R. & Buland, R., 1995. Constraints on seismic velocities in the Earth from traveltimes, *Geophys. J. Int.,* **122**(1), 108–124.

Lim, H., Kim, Y.H., Clayton, R.W. & Thurber, C.H., 2018. Seismicity and structure of Nazca Plate subduction zone in southern Peru, *Earth planet. Sci. Lett.,* **498,** 334–347.

Liu, W. & Yao, H., 2020. Rupture Process of the 26 May 2019 Mw 8.0 northern peru intermediate-depth earthquake and insights into its mechanism, *Geophys. Res. Lett.,* **47**(4), doi:10.1029/2020GL087167.

McGlashan, N., Brown, L. & Kay, S., 2008. Crustal thickness in the central Andes from teleseismically recorded depth phase precursors, *Geophys. J. Int.,* **175**(3), 1013–1022.

Münchmeyer, J., Saul, J. & Tilmann, F., 2023. Learning the deep and the shallow: deep-learning-based depth phase picking and earthquake depth estimation, *Seismol. Res. Lett.,* doi:10.1785/0220230187.

Murphy, J.R. & Barker, B.W., 2006. Improved focal-depth determination through automated identification of the seismic depth phases pp and sp, *Bull. seism. Soc. Am.,* **96**(4A), 1213–1229.

Omohundro, S.M., 1989. Five balltree construction algorithms, *Science,* **51**(1), 1–22.

Pedregosa, F. *et al.*, 2011. Scikit-learn: machine learning in python gaël varoquaux bertrand thirion vincent dubourg alexandre passos pedregosa,

varoquaux, gramfort et al. matthieu perrot, *J. Mach. Learn. Res.,* **12,** 2825–2830.

Portner, D.E. & Hayes, G.P., 2018. Incorporating teleseismic tomography data into models of upper mantle slab geometry, *Geophys. J. Int.,* **215**(1), 325–332.

Rost, S. & Thomas, C., 2002. Array seismology: methods and applications, *Rev. Geophys.,* **40**(3), 2–1.

Sandiford, D., Moresi, L., Sandiford, M. & Yang, T., 2019. Geometric controls on flat slab seismicity, *Earth planet. Sci. Lett.,* **527,** 115787, doi:10.1016/j.epsl.2019.115787.

Schimmel, M. & Paulssen, H., 1997. Noise reduction and detection of weak, coherent signals through phase-weighted stacks, *Geophys. J. Int,* **130,** 497–505.

Schweitzer, J., Fyen, J., Mykkeltveit, S., Gibbons, S., Pirli, M., Kühn, D. & Kværna, T., 2012. Seismic arrays, in *In New Manual of Seismological Observatory Practice 2 (NMSOP-2),* pp. 1–80, Deutsches GeoForschungsZentrum GFZ.

Tibuleac, I.M., 2014. A method for first-order earthquake depth estimation using superarrays, *Seismol. Res. Lett.,* **85**(6), 1255–1264.

Vallée, M. & Douet, V., 2016. A new database of source time functions (STFs) extracted from the SCARDEC method, *Phys. Earth planet. Inter.,* **257,** 149–157.

Wagner, L.S. & Okal, E.A., 2019. The Pucallpa Nest and its constraints on the geometry of the Peruvian Flat Slab, *Tectonophysics,* **762**(2018), 97–108.

Ward, J., Thorne, M., Nowacki, A. & Rost, S., 2023. Upper mantle structure beneath the contiguous US resolved with array observations of SKS multipathing and slowness vector perturbations, *J. geophys. Res.: Solid Earth,* **128**(7), e2022JB026260, doi:10.1029/2022JB026260.

Wimpenny, S., Craig, T. & Blackwell, A., 2023. Lower-crustal normal faulting and lithosphere rheology in the atlas Foreland, *J. geophys. Res.: Solid Earth,* **128**(12), doi:10.1029/2023JB028090.

Woodgold, C. R.D., 1999. Wide-aperture beamforming of depth phases by timescale contraction, *Bull. seism. Soc. Am.,* **89**(1), 165–177.